Journal of Catalysis 307 (2013) 1–17

Contents lists available at SciVerse ScienceDirect

Journal of Catalysis

journal homepage: www.elsevier.com/locate/jcat

Effect of the ZrO_2 phase on the structure and behavior of supported Cu catalysts for ethanol conversion

A.G. Sato [a], D.P. Volanti [b], D.M. Meira [a], S. Damyanova [c], E. Longo [b], J.M.C. Bueno [a,*]

[a] Laboratório de Catalise, Departamento de Engenharia Química, Universidade Federal de São Carlos, C.P. 676, 13565-905 São Carlos, SP, Brazil
[b] Laboratório Interdisciplinar de Eletroquimica e Cerâmica, Departamento de Físico-Química, Instituto de Química Universidade Estadual Paulista, 14800-900 Araraquara, SP, Brazil
[c] Institute of Catalysis, Bulgarian Academy of Sciences, 1113 Sofia, Bulgaria

ARTICLE INFO

Article history:
Received 23 April 2013
Revised 17 June 2013
Accepted 22 June 2013

Keywords:
Ethanol dehydrogenation
Cu/ZrO_2 catalysts
Ethyl acetate
Characterization

ABSTRACT

The effect of amorphous (*am*-), monoclinic (*m*-), and tetragonal (*t*-) ZrO_2 phase on the physicochemical and catalytic properties of supported Cu catalysts for ethanol conversion was studied. The electronic parameters of Cu/ZrO_2 were determined by in situ XAS, and the surface properties of Cu/ZrO_2 were defined by XPS and DRIFTS of CO-adsorbed. The results demonstrated that the kind of ZrO_2 phase plays a key role in the determination of structure and catalytic properties of Cu/ZrO_2 catalysts predetermined by the interface at Cu/ZrO_2. The electron transfer between support and Cu surface, caused by the oxygen vacancies at *m*-ZrO_2 and *am*-ZrO_2, is responsible for the active sites for acetaldehyde and ethyl acetate formation. The highest selectivity to ethyl acetate for Cu/*m*-ZrO_2 catalyst up to 513 K was caused by the optimal ratio of Cu^0/Cu^+ species and the high density of basic sites (O^{2-}) associated with the oxygen mobility from the bulk *m*-ZrO_2.

© 2013 Elsevier Inc. All rights reserved.

1. Introduction

The establishment targets for reducing greenhouse gas emissions that contribute to the global warming should have a significant increase in the consumption of biofuels in coming years, especially ethanol. This requires a substantial increase in ethanol production and, in this sense, encourages research and development of new raw materials for ethanol, such as lignocellulosic biomass, and the construction of integrated bio-refineries, a similar concept to that of oil refineries. Attention also turned to chemical ethanol or ethanol chemistry, as the way to increase the chemical production using a green chemistry route employing renewable resources [1].

Acetaldehyde is a product of ethanol dehydrogenation, which can be used as an intermediate in the production of acetic acid, acetic anhydride, ethyl acetate, butyraldehyde, crotonaldehyde, *n*-butanol, and many other chemicals. Ethyl acetate as one of the main products of ethanol dehydrogenation is an environmentally friendly organic solvent, which can be used for organic synthesis, printing inks, adhesives, and cosmetics.

Copper-based catalysts were found to be excellent catalysts for ethanol dehydrogenation because of their ability to maintain the C–C bond intact while dehydrogenating the CO–H bond [2]. Some investigations have been focused on the effect of support material on secondary product selectivity. In addition to simple dehydrogenation of ethanol, dehydrogenative coupling between the product acetaldehyde and the ethanol could also occur to produce ethyl acetate and hydrogen. Studies have shown that ethyl acetate can be obtained directly from ethanol employing specific heterogeneous catalysts [3–8]. Iwasa and Takezawa [9] examined SiO_2, ZrO_2, Al_2O_3, MgO, and ZnO as support for Cu-based catalysts and found that the selectivity to acetaldehyde or ethyl acetate depends strongly on the support kind. As the ethanol dehydrogenation is an exothermic reaction, there is a formation of hot spots in the reactor which leads to sintering the Cu particles and to decrease in the catalyst activity [8]. ZrO_2 has been described as preventive element for sintering of Cu crystallites under the reaction conditions and therefore was considered as a structural promoter and as an alternative support [10,11]. Recently, rice husk ash (RHA) composed of amorphous silica has been used as a carrier for supported copper catalysts prepared by ion-exchanged, which showed very high Cu dispersion and stability in ethanol dehydrogenation to acetaldehyde at reaction temperature of 483–548 K [12].

Zirconium oxide has received considerable attention as a catalyst and support due to its unique properties; the preservation of both acid and basic sites, on the one hand, and reducing and oxidizing properties, on the other hand. As a result, the use of zirconia rather than silica or alumina as a structural promoter or more frequently as a support material has attracted considerable interest for a number of catalytic applications in the recent years. In partic-

* Corresponding author.
E-mail address: jmcb@ufscar.br (J.M.C. Bueno).

0021-9517/$ - see front matter © 2013 Elsevier Inc. All rights reserved.
http://dx.doi.org/10.1016/j.jcat.2013.06.022

ular, it has been found that the activity of Cu/ZrO_2 catalysts is strongly dependent on the phase structure of ZrO_2. Within this context, it was reported [13] that Cu catalysts supported over *m*-ZrO_2 are more active in methanol synthesis than catalysts with the same Cu surface density deposited on *t*-ZrO_2. The origin of these differences was explained by the presence of higher concentration of anionic defects on *m*-ZrO_2 than on *t*-ZrO_2 [14]. The different spacing and symmetry of the Zr–O and –OH bonds at *t*-ZrO_2 and *m*-ZrO_2 are considered to play key roles in determining the dispersion of the active metal component and the catalytic properties of Cu/ZrO_2 system [14].

The high copper–zirconia interface has been considered as a key for obtaining highly active and selective copper catalysts with improved stability [15]. The surface metallic copper area as well as the kind of supported copper species is also expected to play a vital role in the catalytic systems. A correlation between the surface metallic Cu area and the catalyst activity was found [18]. New type of nanostructured Cu/ZrO_2 materials featured with high component dispersion has been obtained for methanol steam reforming [16].

There are several reports in the literature concerning the ethyl acetate and acetaldehyde formation from ethanol on Cu-based catalysts [9,17,18]. But these reports are not focused on the active catalytic sites. To establish reliable reaction pathways models, the first step is the knowledge of the catalyst active sites, a point of vital importance to understand and predict the catalytic properties, the most ambitious goal in the field of catalysis.

ZrO_2-supported Cu catalysts have been used in many others reactions such as methanol synthesis [14], steam reforming of methanol [19,20], and water–gas shift reaction [21]. Based on the XPS and XAS experiments, it was reported the presence of Cu^+ species in the CuO pathway reduction in Cu/ZrO_2 catalysts [20,22,23]. Also, it was reported [19,20] that quite stable Cu^+ as intermediate Cu species in the CuO reduction were formed as active species in the steam reforming of methanol over Cu/ZrO_2 catalysts, but there was no conclusion whether the partial copper oxidation was due to the Cu/ZrO_2 interaction or to the presence of water. Although there was not directly detection of Cu^+, it was proposed [8] that the presence of a certain amount of Cu^+ species over Cu/ZrO_2 catalyst is very important for improving the selectivity to ethyl acetate.

Understanding the chemistry occurring on the surface of oxide-supported metal clusters provides critical information for the design and development of superior heterogeneous catalysts. At the present, a few information exists in the literature about the direct relation between the electronic properties of copper-based catalysts supported on zirconia and the product selectivity in the ethanol conversion. In the present work for first time, it is attempted to demonstrate that the catalytic behaviors of Cu catalysts supported on different ZrO_2 phases, such as amorphous (*am*-), monoclinic (*m*-), and tetragonal (*t*-), in the reaction of ethanol conversion are directly related to the electronic properties of supported copper species as well as to the specific properties of support. The study reports in detail the physicochemical characterization of Cu/ZrO_2 catalysts in relation to their structure and acid–base properties as a function of the support kind. The influence of the ethanol pressure, the contact time, and the reaction temperature on the rate of ethyl acetate and acetaldehyde formation as well as on the product selectivity is clarified. To gain insight into the nature of supported copper species and supports, extensive characterization was carried out by: N_2 adsorption, X-ray diffraction (XRD), X-ray photoelectron spectroscopy (XPS), diffuse reflectance Fourier transform infrared spectroscopy of CO adsorption (DRIFTS), temperature-programmed reduction (TPR), in situ X-ray absorption near edge structure (XANES), and extended X-ray absorption fine structure (EXAFS) spectroscopy.

2. Experimental

2.1. Catalyst preparation

Amorphous ZrO_2 was prepared by sol–gel method described in Ref. [24]. Zirconium *n*-propoxide ($Zr(OCH_2CH_2CH_3)_4$ (10.9 ml, 70% in propanol) was dissolved in 233 ml anhydrous ethanol to obtain a 0.1 M solution. Deionized water was added dropwise to the zirconium *n*-propoxide solution to give water/alkoxide ratios of 32. A cloudy solution was obtained on the initial addition of water, which turned to a white suspension on complete addition. The suspension was aged at room temperature for 24 h, followed by the removal of the solvent by rotary evaporation. The obtained wet solid was suspended in 350 ml deionized water with pH adjusted to 10 with ammonium hydroxide (NH_4OH, 30% in volume) and then was refluxed at 373 K in a 500 ml round-bottomed flask. The pH was maintained constant throughout the entire digestion that was a period of 240 h. The solid was washed with deionized water. The samples were dried at 373 K overnight and successively calcined from room temperature to 673 K at a heating ramp of 10 K/min and a dwell time of 5 h under synthetic air flow (100 ml/min). Monoclinic and tetragonal ZrO_2 commercial grades (Saint-Gobain NorPro) were used as supports.

Cu/ZrO_2 samples were prepared by incipient wetness impregnation of the supports with a solution of $(Cu(NO_3)_2{\cdot}2.5H_2O$, 98%; Aldrich) in methanol. The mixture was stirred in a round-bottomed flask under ultrasonic bath coupled with a rotary evaporation. The solids were dried at 373 K overnight and calcined from room temperature to 673 K at a heating ramp of 10 K/min and a dwell time of 5 h under synthetic air flow (100 ml/min). The theoretical amount of Cu was about 10 wt%. Cu supported on *am*-ZrO_2, *m*-ZrO_2 and *t*-ZrO_2 here referred as Cu/*am*-ZrO_2, Cu/*m*-ZrO_2 and Cu/*t*-ZrO_2, respectively.

2.2. Methods

The crystallographic phase of supports and Cu catalysts was achieved by XRD. XRD patterns were collected by Rigaku DMax 2500PC, 40 kV e 150 mA, using Cu Kα (λ = 1.5406 Å) radiation. The data were collected from 20° to 45° in 2θ range with 0.5° divergence slit, 0.3 mm receiving slit, in fixed-time mode with 0.02° step size.

Specific surface area (S_{BET}) and pore volume (V_p) of the samples were determined from the corresponding nitrogen adsorption–desorption isotherms measured at 77 K on an ASAP2010 apparatus (Micromeritics, Norcross, GA, USA).

TPR profiles of the samples were performed with a Micromeritics Pulse Chemisorb 2705. A flow of 10% H_2/He (30 ml/min) was passed through the sample, and the temperature was raised at a rate of 10 K/min up to 523 K, while the thermal conductivity detector (TCD) signal was recorded.

XPS data were obtained with an SPECSLAB II (Phoibos-Hsa 3500 150, 9 channeltrons) SPECS spectrometer, with Al Kα source (E = 1486.6 eV) operating at 15 kV, Epass = 40 eV, 0.05 eV energy step and acquisition time of 1 s per point. The samples were placed on stainless steel sample-holders and were transferred to the XPS pre-chamber under inert atmosphere and stayed there for 12 h in a vacuum atmosphere. The residual pressure inside the analysis chamber was smaller than 1×10^{-9} Torr. The binding energies (BE) were referenced to the C 1s peak at 284.6 eV, providing accuracy within ±0.2 eV. All samples were reduced in a furnace from room temperature to desired temperature according to H_2-TPR behavior at 10 K/min, staying at 503 K for 30 min under a 60 ml/min flow rate of 5% H_2/He, and then cooled to room temperature to precede subsequent analysis.

In the same TPR apparatus described above, N_2O titration was used to determine the surface area of dispersed metallic copper (Cu^0). The Cu/ZrO_2 samples were reduced up to 523 K and after that were cooled to 303 K and exposed to 1% N_2O/He (30 ml/min) for 10 min. It was expected that neither of the ZrO_2 supports exhibits a significant interaction with N_2O at that temperature [17]. A second H_2-TPR by increasing the temperature up to 773 K at a rate of 10 K/min under 5% H_2/He was acquired. The hydrogen consumption was used to calculate the amount of oxygen deposited after N_2O titration. A total of 1.46×10^{19} Cu atoms/m^2 and a stoichiometry of $2Cu/H_2$ were used [25]. No significant bulk oxidation was observed for the samples. The Cu^0 surface area was calculated on the basis of the following relationship in:

$$SA_{Cu} = 6.4955 \times 10^{-2} \times C \times D \quad (1)$$

where C is Cu content (%) and D is Cu^0 dispersion (%).

In situ XANES spectra at the Cu K-edge were carried out at the D06A-DXAS beamline of the Brazilian Synchrotron Light Laboratory (LNLS) at Campinas-SP, Brazil. The D06A-DXAS beamline is equipped with a focusing curved Si (1 1 1) monochromator, operating in Bragg mode, for the selection of the desired range of X-ray wavelengths (8900–9400 eV). The samples were prepared as self-supporting pellets containing ~25 mg of catalyst and placed into a tubular quartz furnace (di = 20 mm and X-ray path length = 440 mm) sealed with kapton refrigerated windows for the transmission measurements. Temperature-resolved XANES spectra at the Cu K-edge were acquired during TPR under a 5% H_2/He flow, heating from room temperature up to 800 K at 10 K min^{-1} (named XANES-TPR). The information about the proportion of the CuO, Cu_2O and Cu metal evolution in the H_2-TPR experiments to Cu/ZrO_2 polymorphs was achieved by the linear combination fitting (LCF) method. In the LCF method, the X-ray absorption spectrum is modeled by least-squares fitting using a linear combination (LCF) of known species (patterns) to fit an unknown spectrum (samples).

EXAFS spectra were carried out at the D04B-XAFS1 beamline of LNLS. This bending magnetic beamline is equipped with a (1 1 1) silicon channel cut monochromator and allowed us to perform EXAFS measurements. Spectra were acquired at room temperature from samples reduced in H_2 at 523 K. The EXAFS signal was extracted in a standard way using Athena/Artemis software packages. The fits were done fixing the same passive electron amplitude reduction factor (*S02*) and photoelectron energy origin correction (ΔE_0) found for the references compounds. The coordination number of the path (N_i), the effective half-path length, R_i (which is equal to the inter-atomic distance for single-scattering paths), and the Debye–Waller factor, σ_i^2, were the parameters that were adjusted. The local environment of the Cu atoms was determined from the EXAFS using the phase shift and amplitude function for Cu–Cu and Cu–O calculated including multiple scattering processes (FEFF version 6.0). The oscillations were weighted with k^2 and Fourier transformed within the limit k = 3.5–12 $Å^{-1}$. The procedure to prepare the sample was the same used on DXAS beamline. The relatively narrow fitting range Δk, was used in the present catalyst systems, since the Hf L_3-edge (9651 eV) due to HfO_2 (present as an impurity in the ZrO_2 used) severely hampers extraction of Cu K-edge oscillations at higher k values [26].

Based on EXAFS data and considering copper particles in cuboctahedral model [27], the Cu^0 surface area was calculated on the basis of (Eq. (1)) combined with the following relationship:

$$N_{Cu-Cu} = \frac{24L(5L^2 + 3L + 1)}{10L^3 + 15L^2 + 11L + 3} \quad (2)$$

$$D_{Cu} = \frac{30L^2 + 6}{10L^3 + 15L^2 + 11L + 3} \quad (3)$$

where N_{Cu-Cu} is the coordination number of Cu cluster; L is the copper cluster order; and D_{Cu} is the dispersion related to the number of Cu atoms in a crust per total number of atoms in a cuboctahedral cluster.

The particle size d_p of copper cluster was calculated according to the (Eq. (2)):

$$D_p = LR_{Cu-Cu} \quad (4)$$

where R_{Cu-Cu} is the inter-atomic distance between copper–copper.

The diffuse reflectance FTIR spectra of adsorbed CO were recorded using a Thermo Nicolet 4700 Nexus FTIR spectrophotometer with MCT detector and a (DRIFTS) reactor cell Spectra Tech with CaF_2 windows (DRIFT HTHV cell). IR spectra were collected in 64 scans at 4 cm^{-1} resolution. The samples were dried at 473 K in a He flow during 1 h, followed by reduction at 503 K in a flow of 34% H_2/He mixture for 2 h. The CO was introduced for 1 s and adsorbed at 323 K at CO pressure of 20 Torr. Temperature-programmed desorption (TPD) of adsorbed CO was carried out in flowing He (30 ml/min) with a heating rate of 10 K/min.

2.3. Catalytic test

Activity and selectivity measurements for ethanol reaction were carried out in a continuous-flow, tubular fixed-bed glass reactor (10 mm i.d.) over the temperature range of 473–548 K at atmospheric pressure. Samples were reduced in situ by heating in pure H_2 flow from room temperature to 503 K at 10 K/min staying at this temperature for 1.5 h. Attempting to analyze the effect of ethanol partial pressure on the reaction, first experiments were carried out isothermally at 473 K with catalyst weight of 0.2 g at high ethanol conversion at contact time of W/F = 38 min, where W and F correspond to catalyst weight (g) and flow rate of ethanol (g/min), respectively. Ethanol (99.9%) in gas phase was fed to catalytic reactor by passing He flow through a saturator submerged in a water bath with temperature at 296, 313, 328, and 338 K, allowing a partial pressure of ethanol feeding of 7.0, 17.9, 37.4, and 58.6 kPa, respectively. The helium gas flow was adjusted keeping a constant flow of reagent dragged into the reactor for all partial pressures of analyzed ethanol. The temperature-resolved reactions were performed with catalyst of 0.04 and 0.2 g at low and at high ethanol conversion at low and high contact time of W/F = 1.2 min and 38.0 min, respectively. Reaction products were collected periodically and analyzed by online gas chromatography (Varian GC-3400 CX) with a Chromosorb 102 column. Conversion and selectivity were determined on the carbon basis products. Turnover frequencies (TOFs) of acetaldehyde and ethyl acetate formation using the Cu metal surface area per gram of catalyst based on N_2O titration data ($TOFs_{(N2O)}$) and EXAFS analysis ($TOFs_{(EXAFS)}$) were calculated. The extent of ethanol conversion was maintained below 15%.

3. Results

3.1. XRD

XRD patterns of pure ZrO_2 supports and calcined Cu/ZrO_2 samples are shown in Fig. 1. Intensive diffraction patterns at 2θ = 24.2°, 28.2°, 31.4°, and 34.3° of monoclinic ZrO_2 crystal phase (JCPDS 37-1484) are predominant for Cu/*m*-ZrO_2. In addition to the characteristic peaks of zirconia, XR diffractions at 2θ = 35.5° and 38.7° are detected for Cu/*m*-ZrO_2, corresponding to crystalline CuO phase with tenorite structure (JCPDS 48-1548). The absence of crystalline CuO peaks in the XRD of Cu/*am*-ZrO_2 and Cu/*t*-ZrO_2 samples cannot be ruled out as they might be less than 4 nm in size, which is beyond the detection capacity of the XRD technique. A broad X-ray

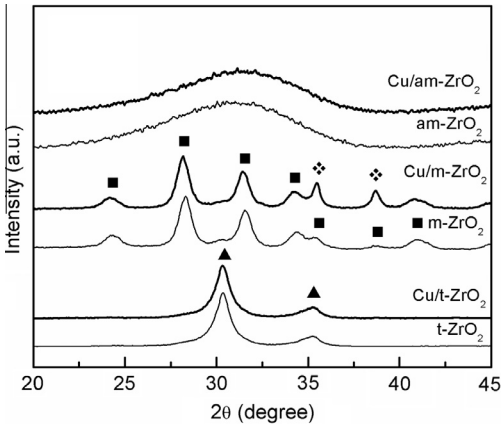

Fig. 1. XRD of ZrO_2 polymorphs and Cu/ZrO_2 catalysts: *m*-ZrO_2 (■); *t*-ZrO_2 (▲), and CuO (❖).

diffraction patterns are observed for *am*-ZrO_2 sample, pointing to an amorphous or disordered at long range nature of zirconia. For Cu/*t*-ZrO_2, diffraction peaks at $2\theta = 30.3°$ and 35.4° of *t*-ZrO_2 crystal phase (JCPDS 50-1089) are detected.

3.2. Textural properties

Some textural characteristics of the supports and Cu/ZrO_2 samples are listed in Table 1. The Cu^0 surface area (SA_{Cu}) and the corresponding apparent Cu^0 dispersion (D_{Cu}) for each sample obtained by N_2O titration method and from EXAFS analysis are also given in the Table 1. The S_{BET} values of calcined Cu/ZrO_2 samples are lower compared to those of the pure supports. Within the zirconia supports, series *am*-ZrO_2 has the highest specific surface area.

The data N_2O titration and EXAFS analysis in Table 1 demonstrate that the Cu/*t*-ZrO_2 exhibits the highest apparent Cu^0 dispersion. Similar results have been observed by Rhodes and Bell [14], who assigned the lower Cu^0 dispersion on *m*-ZrO_2 to a higher point of zero charge of 8.5 and charge density of the monoclinic polymorph [28]. The net positive charge at the surface of *m*-ZrO_2 leads to a weaker interaction between the support and Cu species [28], which contributes to a lower dispersion and formation of bulk CuO as was detected by the XRD in Fig. 1.

3.3. XPS analysis

XPS of Cu 2p and Auger peak, Zr 3d and O 1s core electron level of reduced Cu/ZrO_2 samples are shown in Fig. 2A, B, C, and D, respectively. The XPS parameters are summarized in Table 2. All reduced samples exhibit symmetric Cu $2p_{3/2}$ and Cu $2p_{1/2}$ main peaks (Fig. 2A) with BEs values at ca. 932.5 and 952.4 eV, respectively, with a spin–orbit coupling energy of 20 eV. A shake-up satellite at about 942 eV was not detected, which suggests the absence of Cu^{2+} species [29]. It should be noted that the satellite peaks are not seen in the case of Cu^+ or Cu^0 species because of completely filled 3d shells. The FWHM of Cu $2p_{3/2}$ is 2.0–2.4 eV, which suggests the presence of at least two kinds of surface copper species different in their chemical environments. Therefore, it cannot be excluded traces of other species, like Cu^+, since the BE of Cu^+ generally overlaps with that of Cu^0 in Cu 2p core level.

To distinguish better Cu^0 from Cu^+ species, having similar BE, the X-ray induced Auger electron spectra of reduced samples in the kinetic region of 928–902 eV are presented in Fig. 2B. A clear difference is observed in the shapes of Cu $L_3M_{45}M_{45}$ Auger photoelectron spectra of the samples, being in agreement with those previously reported in the literature for Cu^0 and Cu^+ species [29]. The reported changes have been attributed to the specific bonding interactions appearing at the interface between the two oxide phases species. Peaks at ca. 918.4 and ca.915.5 eV are detected, which characterize Cu^0 and Cu_2O, respectively [29]. In the Auger spectra, the position of the main peak for Cu/*am*-ZrO_2 sample at about 915.6 eV is shifted to a higher kinetic energy, up to 918.4 eV for Cu/*t*-ZrO_2, which is usually assigned to the increase inf Cu^0 amount. The latter is in agreement with the highest Cu^0 surface area detected over *t*-ZrO_2 (Table 1). The modified Auger parameter (α_{Cu}) was calculated to determine more precisely the chemical state of copper. This parameter is defined by [29]:

$$\alpha_{Cu} = E_B + E_K \quad (5)$$

where E_B is the binding energy of Cu 2p core level and E_K is the kinetic energy of the Cu LMM Auger electron. The α_{Cu} values at ca. 1851.0 and 1848.1 eV (Table 2) correspond to Cu^0 and Cu^{1+} species, respectively. The α_{Cu} value of 1851.0 eV obtained for reduced Cu/*t*-ZrO_2 sample means that the prevailing species over catalyst surface is Cu^0, whereas the value of ca. 1848.1 eV suggests that Cu^+ is a dominant species for reduced Cu/*am*-ZrO_2 (Table 2 and Fig. 2B). The both features at 1848.0 and 1850.8 eV correlate with the presence of Cu^+ and Cu^0 species, respectively, over *m*-ZrO_2. It is clear that the KE of α_{Cu} increases as a function of the amount of Cu^0, similar to the observations in Ref. [29]. It is interesting to note that for Cu^0 and Cu_2O, the changes in α_{Cu} are larger than those of BE [22].

All samples exhibit a spin–orbit doublet of the Zr 3d core level into $3d_{5/2}$ and $3d_{3/2}$ levels with an energy gap of 2.4 eV between them and a relative intensity ratio (I $3d_{5/2}$/I $3d_{3/2}$) of 1.5 (Fig. 2C). This indicates the existence of ZrO_2-like species according to the literature data [30]. Decomposition of the spectra produces peaks attributed to the existence of two kinds of zirconium species, referred as species I with low BE in the range 181.9–182.4 eV (Zr_I) and species II with higher BE in the range 183.2–183.9 eV (Zr_{II}) (Table 2). It should be noted that the fraction of Zr_I species for all samples is larger compared to that of species Zr_{II}. The BEs of Zr_I are similar to that of Zr^{4+} ions in pure zirconia, but with slightly lower values compared to that of stoichiometric ZrO_2 (182.6 eV), especially for sample Cu/*am*-ZrO_2 (181.9 eV), probably, due to some

Table 1
Textural characteristics for supports and Cu/ZrO_2 catalysts, surface metallic area (SA_{Cu}) and apparent metallic dispersion of Cu (D_{Cu}) based on N_2O titration and EXAFS analysis.

Samples	S_{BET} (m^2/g_{cat})	V_p (cm^3/g_{cat})	N_2O SA_{Cu} (m^2/g_{cat})	Data D_{Cu} (%)	EXAFS[a] SA_{Cu} (m^2/g_{cat})	Data D_{Cu}[b] (%)
am-ZrO_2	376	0.59	–	–	–	–
m-ZrO_2	92	0.28	–	–	–	–
t-ZrO_2	152	0.19	–	–	–	–
Cu/*am*-ZrO_2	265	0.43	14	22	52.4	80.7
Cu/*m*-ZrO_2	76	0.22	13	20	37.6	57.8
Cu/*t*-ZrO_2	115	0.13	22	34	58.6	90.2

[a] Assuming cuboctahedral model;
[b] Number of atoms in a crust per total number of atoms.

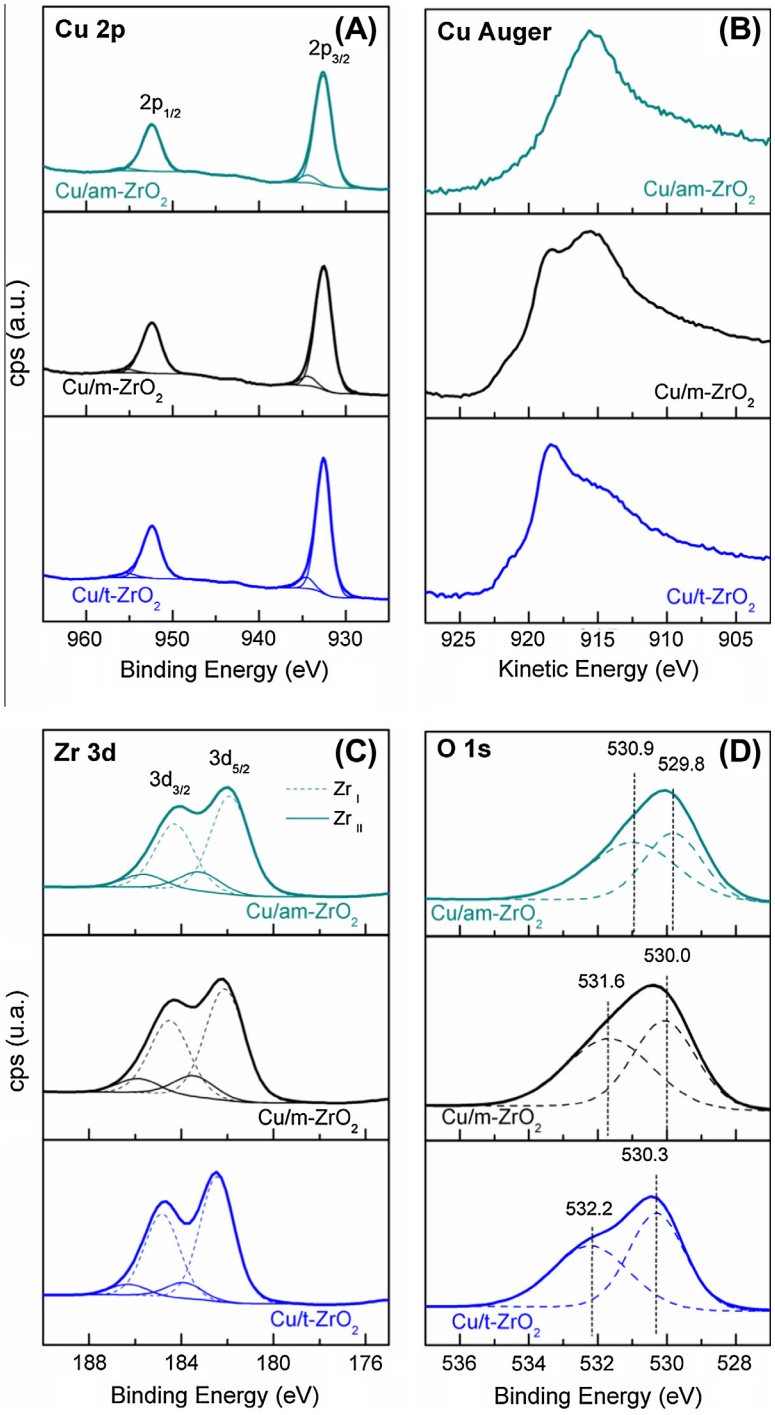

Fig. 2. XPS of Cu 2p (A), Cu Auger (B), Zr 3d (C), and O 1s core level (D) for reduced Cu/ZrO_2 samples.

Table 2
XPS parameters of reduced Cu/ZrO_2 samples.

Samples	Cu $2p_{3/2}$ (eV)	Cu Auger (eV)	α_{Cu} (eV)	Zr $3d_{5/2}$ (eV)		O 1s (eV)		Cu/Zr
				Zr_I species	Zr_{II} species	O_I species	O_{II} species	
Cu/*am*-ZrO_2	932.5 (2.4)[a]	915.6	1848.1	181.9 (83)[b]	183.2 (17)[b]	529.8 (44)[b]	530.9 (56)[2]	0.40
Cu/*m*-ZrO_2	932.5 (2.3)	915.5/918.3	1848.0/1850.8	182.1 (83)	183.4 (17)	530.0 (49)	531.6 (51)	0.49
Cu/*t*-ZrO_2	932.6 (2.0)	918.4	1851.0	182.4 (88)	183.9 (12)	530.3 (53)	532.2 (47)	0.64

[a] Full width at half maximum (FWHM).
[b] Percent of Zr and O species.

oxygen deficiency. The position shift toward the lower binding energy might be associated with the holes created by oxygen vacancies in the ZrO_2 lattice [31]. The BEs of the higher energy component (183.2–183.9 eV) correspond to the formation of a Zr species bound to a more electron attractive species and formation of partially reduced $Zr^{\delta+}$ sites [30].

The value of XPS atomic Cu/Zr ratio for reduced Cu/ZrO_2 samples increases in the following order: $Cu/am\text{-}ZrO_2 > Cu/m\text{-}ZrO_2 > t\text{-}ZrO_2$ (Table 2). The highest Cu/Zr ratio value of 0.64 for $Cu/t\text{-}ZrO_2$ means a pronounced Cu enrichment on the $t\text{-}ZrO_2$ surface. As is shown in Table 1, the highest apparent Cu^0 density and Cu^0 surface area measured by N_2O titration are found for $Cu/t\text{-}ZrO_2$ sample.

The changes in the XPS of O 1s core electron of reduced Cu/ZrO_2 samples can be explained by the superposition of contributions from the substrate and deposited overlayers, as shown in Fig. 2D. The O 1s broad peaks can be decomposed in two peaks at the corresponding position using XPS peak splitting program (XPS Casa Software), whose relative contents are shown in Table 2. According to the literature [31,32], there might be two types of oxygen species in the Cu/ZrO_2 system after reduction: oxygen species of ZrO_2 and/or Cu_2O (O_I) and oxygen species of Zr–OH (O_{II}), whose binding energy is in the range of 529.8–530.3 eV and 530.9–532.2 eV, respectively (Table 2). It was shown that the oxygen species with BE $\geqslant$531.0 eV are attributed to OH, chemisorbed oxygen or carbonates groups [33].

3.4. TPR

Fig. 3 shows that the TPR profiles of calcined Cu/ZrO_2 samples depend on the kind of ZrO_2 phase. TPR of $Cu/am\text{-}ZrO_2$ shows a broad intensive heterogeneous peak ranging from 415 to 480 K with a maximum at 454 K and a shoulder at ca. 440 K. Similarly, $Cu/t\text{-}ZrO_2$ exhibits also an intensive peak but in the lower temperature region; there is a peak at 440 K with a shoulder at 418 K. In addition, a small peak at 477 K is appeared in the TPR of $Cu/t\text{-}ZrO_2$.

Similar reduction peaks for Cu/ZrO_2 samples have been previously observed. It has been found [34,35] that the presence of Cu oxide species differently interacted with the ZrO_2 matrix, depending on the CuO dispersion and crystallinity as well as on the ZrO_2 phase. Usually, dispersed CuO is reduced more easily than larger CuO particles. Comparing the TPR profiles of $Cu/am\text{-}ZrO_2$ and $Cu/t\text{-}ZrO_2$, it can be concluded that supported Cu oxide species on $t\text{-}ZrO_2$ are more easily reduced than that over $am\text{-}ZrO_2$.

In contrast to the TPR profiles of the above-mentioned samples, the TPR of $Cu/m\text{-}ZrO_2$ exhibits more heterogeneous distribution of Cu oxide species (Fig. 3). Reduction peaks for $Cu/m\text{-}ZrO_2$ could be divided in two well defined regions: (i) a lower temperature region (from 400 to 425 K), attributed to the reduction in small copper oxide particles, and (ii) a higher temperature region (from 450 to 530 K) assigned to highly dispersed copper species in a strong interaction with the support as well as to well crystallized CuO in weak interaction with ZrO_2. It can be suggested that there is an intimate contact between Cu and Zr for $Cu/m\text{-}ZrO_2$ sample, which facilitates the reduction in supported copper oxide species at lower temperatures.

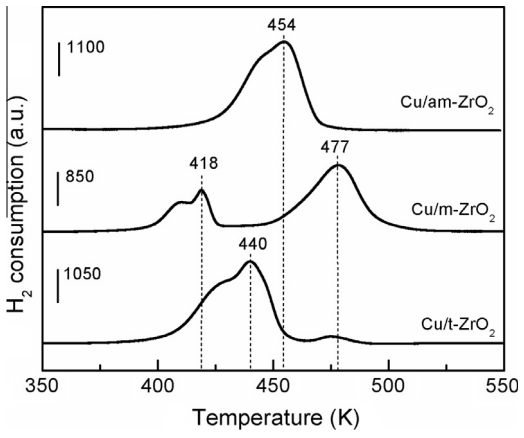

Fig. 3. TPR profiles of calcined Cu/ZrO_2 samples.

The TPR findings indicate the presence of Cu–Zr interaction in the samples in different levels as well as distinct active sites behavior where highly dispersed copper oxide species, crystallized copper oxide strongly or weakly interacted with the ZrO_2 surface coexist.

3.5. In situ XANES analysis

The change in the chemical state and local symmetry of copper is clarified by analyzing the normalized (Fig. 4A) and first derivative (Fig. 4B) of Cu K-edge XANES spectra of calcined Cu/ZrO_2 samples, including the patterns of CuO and $Cu(OH)_2$ references. Normalized spectra of reduced Cu/ZrO_2 samples at the end of reduction process (800 K) as well as of Cu_2O and Cu metal foil are depicted in Fig 4C. There is a relationship between the position of the pre-edge peak (due to the dipole forbidden $1s \rightarrow 3d$) and the coordination geometry of Cu^{2+} compounds patterns. The comparison between the positions of the pre-edge peak of calcined samples and of Cu^{2+} compounds patterns (Fig. 5A) suggests the following: (i) a square planar geometric coordination for $Cu/m\text{-}ZrO$, analogous to CuO and (ii) an octahedral symmetry for $Cu/am\text{-}ZrO_2$ and $Cu/t\text{-}ZrO_2$, analogous to $Cu(OH)_2$ [36,37]. The energy position of the maximum in the pre-edge peak increases from octahedral to square planar [37]. The peak assigned to the $1s \rightarrow (4p_z + L)$ shake-down transition involving a $1s \rightarrow 4p_z$ transition with simultaneous ligand-to-metal charge transfer (LMCT) is also known as the edge transition. The calcined $Cu/m\text{-}ZrO_2$ sample shows this transition at ca. 8984 eV typically for Cu^{2+} compounds. The edge transition for $Cu/am\text{-}ZrO_2$ and $Cu/t\text{-}ZrO_2$ samples shows a small shift to 8986 and 8985 eV, respectively (Fig. 4A) [38,39].

A strong intensive white line (WL) at ca. 8997 eV assigned to dipole $1s \rightarrow 4p_{xy}$ electron transition [40] is observed for CuO, $Cu(OH)_2$, and calcined Cu/ZrO_2 samples (Fig. 4A). The electron transition for Cu_2O appears at 8996 eV. The observed shoulder at 8990 eV for CuO reference in Fig. 4B could be assigned to the covalence degree of the interaction and/or to a disorder degree of the local structure.

The absorption edge for Cu_2O due to electronic transition $1s \rightarrow (4p_z + L)$ appears at 8981.5 eV, while Cu metal foil exhibits absorption edge at 8979 eV and a well-resolved doublet in the post-edge region (Fig. 4C). The values for CuO, Cu foil, and Cu_2O reference are in a good agreement with those reported in the literature [23,29]. The XANES spectra collected at the highest temperature of reduction (800 K) suggest that the absence of WL and the $1s \rightarrow (4p_z + L)$ electron transition at ca. 8979 eV is an indication and that Cu^0 is the dominant species in reduced Cu/ZrO_2 samples.

Fig. 5(A-C) shows in situ Cu K-edge XANES spectra evaluated during the H_2-TPR of $Cu/am\text{-}ZrO_2$ (A), $Cu/m\text{-}ZrO_2$ (B), and $Cu/t\text{-}ZrO_2$ (C) samples in the photon energy region of 8940–9040 eV. The respective semiquantitative change in the percentage of different Cu species with increasing the reduction temperature within 300–800 K is shown in Fig. 5D–F. The corresponding fits, using a linear combination of CuO, Cu_2O, and Cu foil standards, provided a form to monitor the electronic state of copper species evolution. It is observed that the reduction in copper oxide species on $Cu/t\text{-}ZrO_2$ starts at significantly lower temperature (at 398 K) compared to $Cu/am\text{-}ZrO_2$ and $Cu/m\text{-}ZrO_2$ (at 448 and 443 K, respectively). This correlates with the highest apparent metal dispersion detected for $Cu/t\text{-}ZrO_2$ sample (Table 1). On the other hand, the gradual reduc-

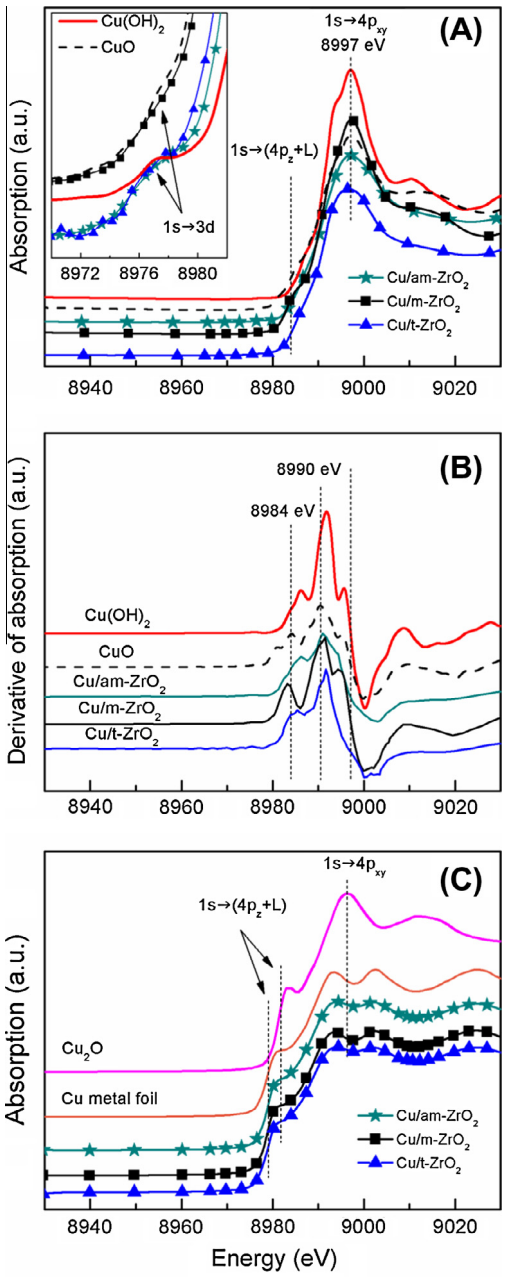

Fig. 4. Normalized XANES spectra at Cu K-edge (A) and respective derivative of XANES spectra of calcined (B) and reduced Cu/ZrO_2 samples (C).

tion in oxide copper species for Cu/*t*-ZrO_2 sample is finished at lower temperature (at 448 K, Fig. 5C) compared to those of the other ones (at 573 and 623 K for Cu/*am*-ZrO_2 and Cu/*m*-ZrO_2, respectively (Fig. 5A and B). It should be noted that all Cu/ZrO_2 samples showed a transition region in which a mixture of three copper species, Cu^{2+}, Cu^+, and Cu^0 is detected, i.e., CuO is reduced to metallic Cu through the intermediate Cu_2O. Similar results have been observed in Ref. [19]. It is interesting to note that a small percentage of Cu^+ species at the end of reduction (up to 800 K) still exists on Cu/*m*-ZrO_2 (Fig. 4E). It means that a more difficult reduction in the Cu oxide species is occurred for Cu/*m*-ZrO_2 sample.

3.6. EXAFS analysis

Fourier transform magnitudes of the experimental EXAFS spectra and respective fits for Cu metal and oxides patterns at Cu K-edge are shown in Fig. S1 (see Supplemental material). The number of neighboring of Cu atoms (N), the distance between them (R), and the statistical order (Debye–Waller factor σ^2) as well as the particles size calculated from the EXAFS analysis are listed in Table 3. The particle size was determined from the average coordination number of the nearest metal neighbor atoms assuming a cuboctahedral geometry [41]. It should be noted that the values of the EXAFS parameters for references CuO, Cu_2O, and Cu^0 are in agreement with those reported in the literature [42]. The values of inter-atomic distances R_{Cu-Cu} for the samples (2.53 ± 0.001 and 2.54 ± 0.002 Å) related to the Cu–Cu distance in bulk Cu^0 indicate that the local structure of supported Cu species is similar to that of Cu^0 (2.54 Å). However, the lower Cu–Cu coordination numbers for supported Cu samples in the range 6.0–9.3 compared to the those of bulk CuO (10) and Cu_2O (12) as well as the different Cu–O bond distances (1.89–1.87 Å) relative to those of bulk CuO (1.94 Å) and Cu_2O (1.84 Å) indicate that the local structure around supported Cu species differs from that of the bulk CuO and Cu_2O. It was shown that the kinetic reductions in Cu/ZrO_2 polymorphs are quite different in relation to unsupported CuO; a direct CuO → Cu transformation occurs on unsupported CuO. Yang et al. [43] showed that both the TPR and isothermal reduction detected easiness in the reduction property of CuO than of Cu_2O under the same reaction conditions. The apparent activation energy for the reduction in CuO is about 14.5 kcal/mol, while for Cu_2O, it is 27.4 kcal/mol [44]. The coordination number of copper particles for Cu/*m*-ZrO_2 (9.3) is the highest in comparison with those for Cu/*am*-ZrO_2 (7.4) and Cu/*t*-ZrO_2 (6), indicating an agglomeration of the copper particles over monoclinic zirconia. The Cu–O bond distance for Cu/*m*-ZrO_2 was not found after reduction, since the EXAFS technique is limited to large particles. It could be supposed that a part of the oxygen species is located on the surface of copper particles according to the observations by Knapp et al. [45]. The authors have showed that the oxygen atoms are located in the tetrahedral or octahedral vacancies of the copper surfaces, and about of one third of the copper surface atoms are blocked by oxygen [45].

3.7. FTIR of CO adsorption

The FTIR spectra of CO adsorption on reduced Cu/ZrO_2 samples in the high frequency (HF) region of 2175–2025 cm^{-1} and in low frequency (LF) region of 1850–1150 cm^{-1} are shown in Figs. 6A–C and D–F, respectively. It is well known [46] that the CO adsorption on copper surfaces exhibits IR bands at 2250–2000 cm^{-1} spectral region associated with the linear or bridge-bonded CO species interacting with CuO, Cu_2O, or Cu^0 sites. The bands at 2116–2111 cm^{-1} have been related to Cu^+-CO carbonyls, while the bands at $\leqslant$2100 cm^{-1} have been assigned to CO-adsorbed on Cu^0 [46].

In the copper spectral region, the IR spectra of reduced Cu/*am*-ZrO_2, Cu/*m*-ZrO_2 and Cu/*t*-ZrO_2 exhibit strong bands with maximum at 2113, 2102, and 2100 cm^{-1}, respectively (Fig. 6A–C). The observed shift in the band maximum of the samples may be caused by changes in the structure and electronic properties of Cu species. According to the literature data [46], the Cu^0–CO carbonyls can be adsorbed at the same frequency, like that of Cu^+–CO ones, when the copper is highly dispersed on the surface. The both species can be better distinguished by their thermal stability criterion: the surface Cu^0–CO carbonyls are easily destroyed with increasing the temperature, while Cu^+ cations form more stable surface carbonyls, being seen in Fig. 6A–C. It should be noted that the high stability of Cu^+–CO species is a result of the stabilization of stronger σ-bond [47]. The adsorbed carbonyl species for Cu samples supported on *am*- and *t*-ZrO_2 are decomposed at higher temperature (at 373 K) in comparison with that supported on *m*-ZrO_2 (at 348 K). Thus, the IR band maximum at 2113 cm^{-1} of Cu/*am*-ZrO_2 sample would be associated with the presence Cu^+–CO carbonyls

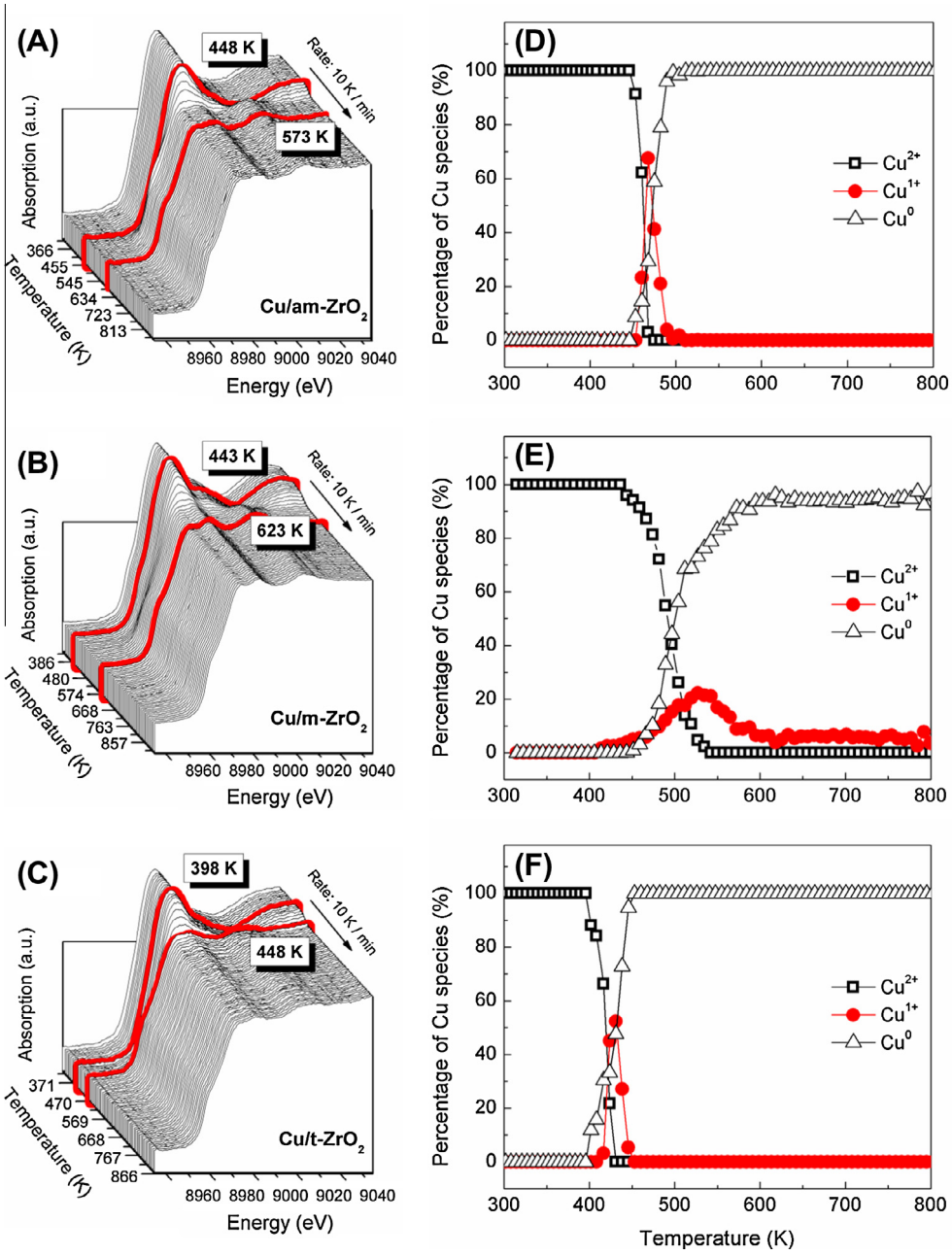

Fig. 5. Temperature-resolved XANES spectra at Cu K-edge of Cu/ZrO_2 samples under hydrogen atmosphere: normalized spectra (A–C) and corresponding percentage of Cu species (D–F).

Table 3
EXAFS parameters of bulk CuO, Cu_2On and Cu^0 references and of $CuZrO_2$ catalysts reduced at 503 K in flow of $5\%H_2$/He.

	References			Samples		
	CuO	Cu_2O	Cu^0	Cu/*am*-ZrO_2	Cu/*m*-ZrO_2	Cu/*t*-ZrO_2
N_{Cu-O}	4	2		0.6		0.7
N_{Cu-Cu}	10	12	12	7.4 ± 0.1	9.3 ± 0.1	6.0 ± 0.1
R_{Cu-O} (Å)	1.94 + 0.006	1.84 + 0.007		1.89 ± 0.01		1.87 ± 0.01
R_{Cu-Cu} (Å)			2.54 + 0.002	2.53 ± 0.001	2.54 ± 0.001	2.54 + 0.001
[a]R_{Cu-Cu} (Å)		3.03 + 0.004		2.67 ± 0.002		2.70 + 0.002
σ^2	0.002 ± 0.001	0.004 ± 0.001	0.009 ± 0.0005	0.008 ± 0.0002	0.009 ± 0.0002	0.008 ± 0.0003
[b]d_P (nm)				4.4	8.7	2.9

[a] Contribution of Cu–Cu bond length for Cu_2O.
[b] d_P: particle size in cuboctahedral model.

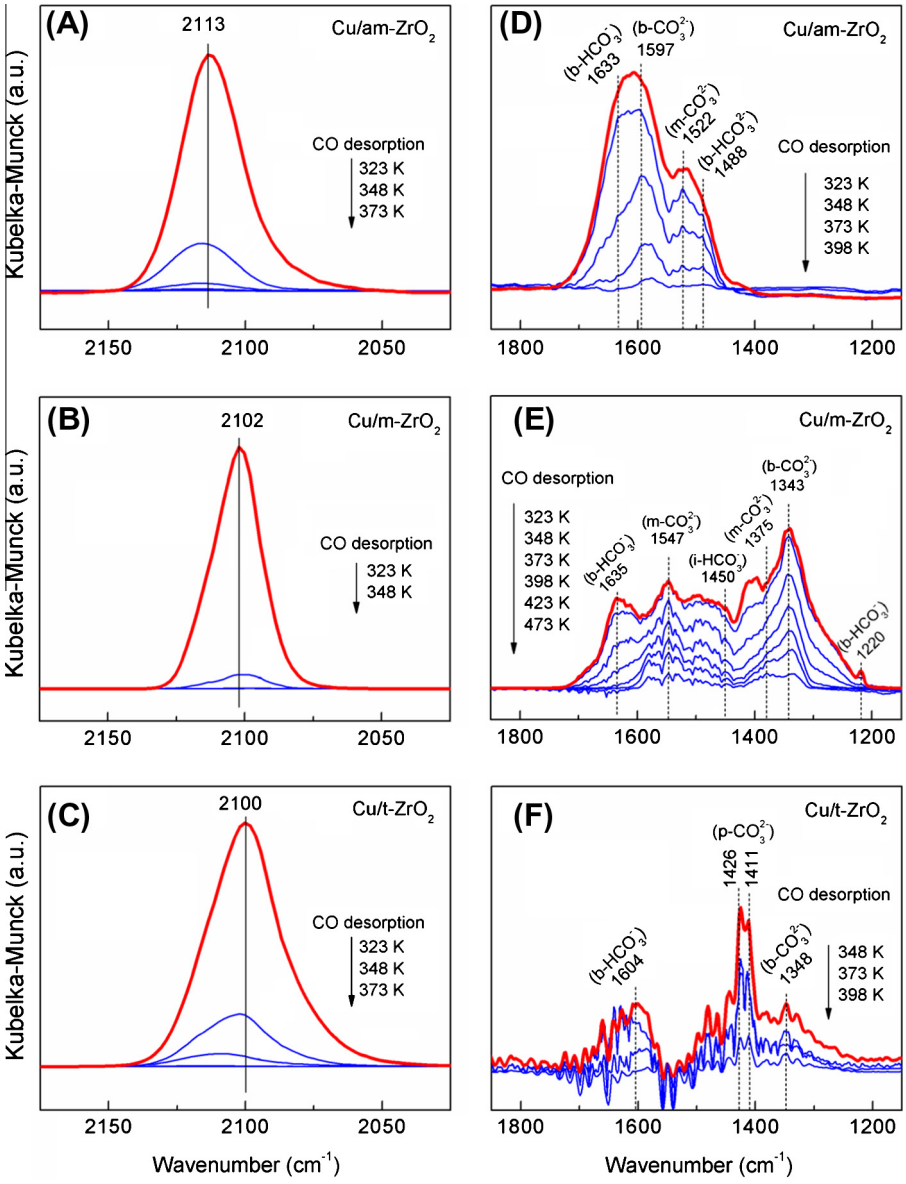

Fig. 6. FTIR spectra of CO adsorption on reduced Cu/ZrO_2 samples in the HF region of 2175–2025 cm^{-1} (A–C) and in LF region of 1850–1150 cm^{-1} (D–F).

as a dominant species. The position of the IR band at ca. 2100 cm^{-1} for Cu/*m*-ZrO_2 and Cu/*t*-ZrO_2 can be related to the adsorbed carbonyls of metallic copper as a prevailing species. However, the carbonyl species on Cu/*t*-ZrO_2 has a slightly higher thermal stability compared to that on Cu/*m*-ZrO_2, which means the presence of copper species with a lower electron density. No Cu^{2+}–CO species were detected in all IR spectra since they usually show bands >2150 cm^{-1} [46].

The CO adsorption capacity on ZrO_2 support as well as the position and intensities of the IR bands in the range of 1850–1150 cm^{-1} depend on the kind of ZrO_2 phase (Fig. 6D–F). The different surface species formed upon CO adsorption can yield information on the existence of surface basic sites (basic OH groups and coordinatively unsaturated sites, *cus* O^{2-} centers) or acid–base pair sites (*cus* Zr^{4+}–O^{2-} centers) [48]. Fig. 6D–F reveals that the band distribution for the three samples is quite different. Following the CO adsorption on Cu/*m*-ZrO_2 sample (Fig. 6E), the following relatively well-resolved bands are observed at 1635, 1547, 1450, 1375, 1343, and 1220 cm^{-1}, which are related to different CO bonded species caused by the presence of acid–base sites. The peaks at 1635 and 1220 cm^{-1} are assigned to bridged bidentate carbonates ($b\text{-}HCO_3^-$), whereas the peaks at ca. 1547 and 1375 cm^{-1} and at ca. 1343 cm^{-1} are related to monodentate ($m\text{-}CO_3^{2-}$) and bidentate ($b\text{-}CO_3^{2-}$) carbonate species, respectively [49–51]. The no well-resolved band at ca. 1450 cm^{-1} can be connected with the formation of ionic carbonate species ($i\text{-}HCO^{3-}$).

Usually, the bicarbonate species are formed by adsorption of CO on basic OH groups. The formation of bicarbonates on *m*-ZrO_2 is connected with the higher fraction of bridged-bonded hydroxyl groups on its surface [51] The above-mentioned both bands corresponding to bidentate carbonates mean different geometrical configurations and/or different crystal planes. The surface bidentate carbonate surface complexes involves acid–base pair sites (*cus* Zr^{4+}–O^{2-} centers), while the monodentate carbonates involve *cus* O^{2-} centers of high basicity [50].

The comparison of the IR spectra of Cu/*m*-ZrO_2 with those of Cu samples supported on *am*- and *t*-ZrO_2 phases (Fig. 6D–F) indicates that for Cu/*am*-ZrO_2, there is a broad band in the higher wavenumber range of 1700–1400 cm^{-1} assigned to $b\text{-}HCO_3^-$, $b-CO_3^{2-}$ and $i\text{-}HCO_2^-$ species. Two kinds of carbonate species are observed for

Cu/*t*-ZrO_2; (i) bidentate carbonate species revealed by the broad band at ca. 1064 cm^{-1} and by the small one at ca. 1348 cm^{-1} and (ii) polydentate carbonate species (p-CO_3^{2-}) [52] detected by the strong bands at ca. 1426 and 1411 cm^{-1}. The p-CO_3^{2-} species is caused by the presence of strong Lewis acid sites due to the closely spaced *cus* Zr^{4+} sites at the *t*-ZrO_2 surface [52].

The effect of ZrO_2 phase on the thermal stability of adsorbed CO is illustrated in Fig. 6D–F, showing TPD of adsorbed CO. The resistance to thermal desorption of CO is a way to qualify the strength and nature of the acid–base sites over Cu/ZrO_2. A band intensity decrease and some displacement in the IR spectra of all samples with increasing the temperature of CO desorption are observed. For CO-adsorbed at 323 K, the CO adsorption capacity on Cu/*m*-ZrO_2 is retained to a significantly higher temperature (up to 473 K) than that on Cu/*t*-ZrO_2 (up to 398 K) and Cu/*am*-ZrO_2 (up to 398 K). It means that CO is bound more strongly on the *m*-ZrO_2 surface revealed by the presence of bands at 1547 cm^{-1}, 1343 cm^{-1}, and at 1375 cm^{-1} assigned to b-CO_3^{2-} and m-CO_3^{2-} species, respectively. It should be noted that the thermal stability of hydrogen carbonates is very limited being eliminated at 373 K.

Most likely, the differences in the CO adsorption capacity and strength on the different ZrO_2 phases are due to differences in the local environment of the OH groups. As was shown in Ref. [14], the difference in the adsorption capacity of CO on Cu/*m*-ZrO_2 and Cu/*t*-ZrO_2 is expected to be a function of the relative concentration of anionic vacancies present on the surface of the two polymorphs of ZrO_2. The higher CO adsorption capacity on *m*-ZrO_2 compared to that on *t*-ZrO_2 might be related to a higher concentration of surface anionic vacancies at the surface of zirconia. Such vacancies expose more *cus* zirconium cations and enhanced the Brönsted acidity of adjacent Zr–OH groups, which are only weak acidic. Thus, the creation of accessible Lewis acid sites in combination with moderately acidic Brönsted acid sites facilitates the adsorption of CO, which is a basic molecule.

3.8. Performance of Cu/ZrO_2 catalysts in the reaction of ethanol conversion

The effect of the partial pressure of ethanol (P_{EtOH}) on the ethanol conversion and products selectivities are listed in Table 4. The main reaction products are acetaldehyde (AcH) and ethyl acetate (EtOAc). By-products of ethanol reaction are also formed, which are methyl ethyl ketone (MEK), butanol (BUT), crotonaldehyde (CROT), diethyl ether (DEE), propanone (PROP) or acetone, ethene (ETE), and others like, CO and CO_2. The conversion values of ethanol for Cu catalysts supported on *am*- and *m*-ZrO_2 phases, practically, do not change with the increase in P_{EtOH}, while for Cu/*t*-ZrO_2, there is a decrease in the conversion. It should be noted that for all catalysts, the selectivity to ethyl acetate increases with the partial pressure at the expense of the acetaldehyde consumption, as the highest values are observed for Cu/*m*-ZrO_2 (Table 4 and Fig. S2). The selectivity to methyl ethyl ketone and crotonaldehyde also decreases with the increase in ethanol partial pressure; the highest selectivity is observed for Cu/*t*-ZrO_2 catalyst (Table 4). Both the Cu/*am*-ZrO_2 and Cu/*m*-ZrO_2 catalysts show low dependence of P_{EtOH} in the crotonaldehyde formation.

It is interesting to note that the total amount of the products (hereafter designed as PCD) formed via acetaldol by aldol condensation (including MEK/BUT and CROT) and the products of ethanol dehydration (including DEE and ETE) [5] are in parallel with the increase in the ethanol partial pressure for Cu catalysts supported on *m*- and *t*-ZrO_2 (Table 4). All catalysts keep a specific relation between the formation of PCD and the water released during the reaction. However, the highest amount of PCD for Cu/*t*-ZrO_2 catalyst does not correspond to a relatively amount of released water like that for Cu/*am*-ZrO_2 and Cu/*m*-ZrO_2 (Table 4). The ratio of water/PCD is different for each catalyst.

Fig. 7 shows the changes in ethanol conversion (A), ethyl acetate selectivity (B), and acetaldehyde selectivity (C) as a function of the reaction temperatures at different contact times at high (W/F = 38 min) and at short contact time (W/F = 1.2 min) and at constant P_{EtOH} = 37.4 kPa. The activity of all catalysts increases with increasing the reaction temperature. The behaviors of Cu/ZrO_2 catalysts at temperatures ranging from 473 to 548 K are equivalent in terms of ethanol conversion for both the short and high contact time (Fig. 7A). However, concerning the selectivity to acetaldehyde and ethyl acetate a great difference is observed for zirconia-supported Cu catalysts at different contact times. The reaction prioritizes the ethyl acetate formation at high contact time (Fig. 7B), whereas acetaldehyde is readily formed at short contact time (Fig. 7C). It should be noted that the effect of the kind of ZrO_2 phase has a strong influence on the product selectivity. The selectivity to ethyl acetate of Cu/*m*-ZrO_2 catalyst at 473–523 K is higher compared to those of Cu supported on *am*- and *t*-ZrO_2 at high contact time. However, there is a marked decrease in the selectivity to ethyl acetate for Cu/*m*-ZrO_2 catalyst at temperature above 548 K (from 72.5–73.1% to 57.3%, Fig. 7B). The highest selectivity to acetaldehyde at short contact time is observed for Cu/*am*-ZrO_2 catalyst at reaction temperature of 473 K (80.1%), followed by Cu/*t*-ZrO_2 and Cu/*m*-ZrO_2 (Fig. 7C).

Table 4
Effect of the partial pressure of etanol (P_{EtOH}) on conversion and selectivity of Cu/ZrO_2 catalysts. Catalytic test at T_{reac} = 573 K and W/F = 38 min.

Catalysts	P_{EtOH} (kPa)	X (%)	Selectivity (%)								Quantity (mol)		Ratio
			AcH	EtOAc	MEC[a]	CROT	DEE	PROP	ETE	Others[b]	Total PCD	H_2O	H_2O/PCD
Cu/*am*-ZrO_2	7.0	44.9	43.9	49.2	6.6	–	–	0.2	–	0.1	60.3	271.0	4.5
	17.9	50.1	31.5	61.7	6.2	–	–	0.3	0.1	0.2	130.1	409.9	3.2
	37.4	52.0	23.9	69.6	4.8	0.7	0.4	0.2	0.1	0.3	100.9	339.7	3.4
	58.6	48.0	20.7	72.6	5.1	0.2	0.5	0.4	0.2	0.3	55.9	227.1	4.1
Cu/*m*-ZrO_2	7.0	46.2	40.7	54.8	3.2	0.3	–	0,9	–	0.1	40.6	126.6	3.1
	17.9	46.8	29.1	66.8	2.6	0.6	0.6	–	–	0.3	81.6	274.8	3.4
	37.4	47.7	21.3	75.0	1.9	0.7	0.4	0.4	–	0.3	108.5	499.5	4.6
	58.6	48.9	15.6	80.5	1.6	1.2	0.3	0.5	–	0.3	160.4	741.3	4.6
Cu/*t*-ZrO_2	7.0	56.9	54.1	27.1	13.8	3.7	0.7	0.3	0.2	0.1	200.6	541.4	2.7
	17.9	48.1	44.3	33.1	13.2	8.2	0.5	0.3	0.2	0.2	520.8	1148.7	2.2
	37.4	45.1	35.5	41.0	12.2	10.1	0.5	0.3	0.2	0.2	913.2	2017.8	2.2
	58.6	43.0	29.7	46.9	11.1	11.1	0.3	0.3	0.2	0.4	1188.3	2688.5	2.3

[a] And/or butanol (BUT).
[b] Others: CO and CO_2. Abbreviations: ethanol conversion (X); acetaldehyde (AcH); ethyl acetate (AcOEt); methyl ethyl ketone (MEK); crotonaldehyde (CROT); diethyl ether (DEE); propanone (PROP); ethene (ETE); and products of condensation and dehydration (PCD).

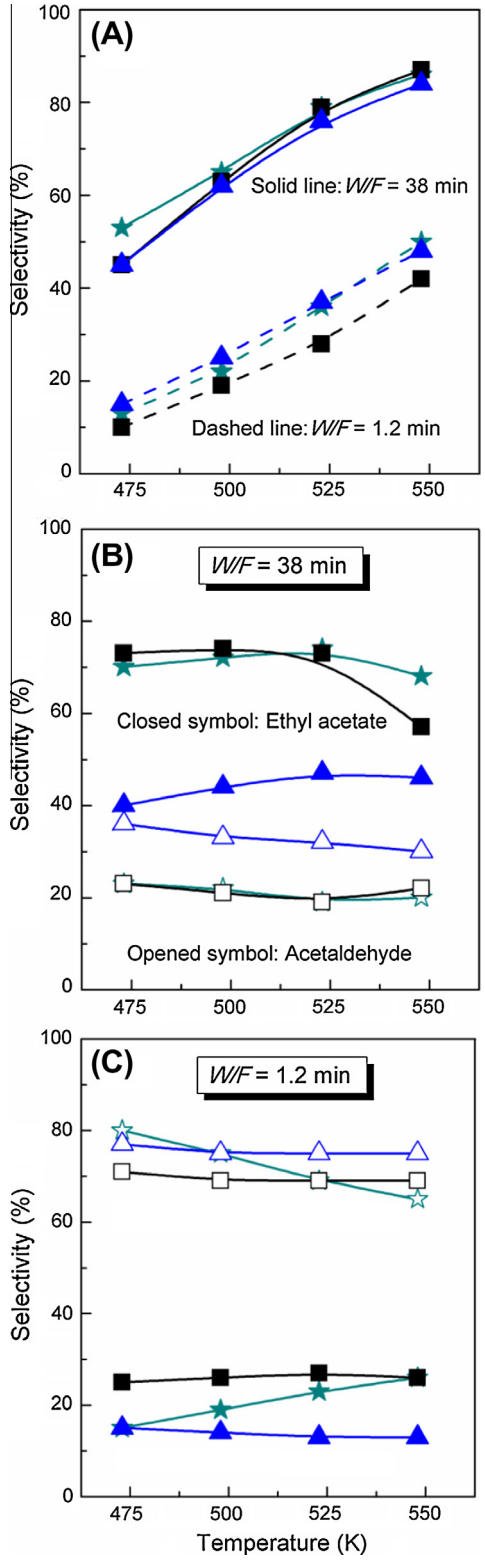

Fig. 7. Effect of the contact time on the ethanol conversion (A), product selectivity at high contact time (F/W = 38 min) (B) and at short contact time (F/W = 1.2 min) (C) as a function of the reaction temperature for Cu/ZrO_2 catalysts: Cu/*am*-ZrO_2 (★) Cu/*m*-ZrO_2 (■) and Cu/*t*-ZrO_2 (▲). (P_{EtOH} = 37.4 kPa).

There is a similarity in the behavior of Cu/ZrO_2 catalysts in relation to methyl ethyl ketone/butanol and crotonaldehyde selectivity (Table 4). Even though these by-products of acetaldehyde condensation should not be formed at short contact time, the Cu/ZrO_2 catalysts showed active sites for methyl ethyl ketone/butanol and crotonaldehyde formation. An increase in the selectivity to products of acetaldehyde condensation with increasing the reaction temperature at short contact time is observed (Fig. S3). In opposite to that, these by-products for Cu/*t*-ZrO_2 catalyst decay pronouncedly with increasing the reaction temperature at high contact time (Fig. 8A and B).

Fig. 9 shows the rate of the formation of acetaldehyde and ethyl acetate at short contact time (over a range of levels at steady state) as a function of the reaction temperature. At all reaction temperatures, the Cu/*t*-ZrO_2 catalyst demonstrates the highest rates in the dehydrogenation of ethanol to acetaldehyde. On the other hand, the same catalyst shows the lowest rate of the ethyl acetate formation. The highest rate of ethyl acetate formation is observed for Cu/*m*-ZrO_2 up to 513 K. However, at temperature above 513 K, the Cu catalyst supported on *am*-ZrO_2 exhibits a strong increase in the rate of ethyl acetate formation.

The apparent activation energy (E_a) of acetaldehyde and ethyl acetate formation (Table 5) was calculated from the slop of Arrhenius plots (Fig. S4). A major E_a for ethyl acetate formation is obtained for Cu/*am*-ZrO_2 catalyst, which means that the reaction rate is very sensible to the temperature, being revealed by the highest inclination of the Arrhenius curve (Fig. S4, B). Cu/*t*-ZrO_2 displays the lowest E_a for both the acetaldehyde and ethyl acetate formation, which means a low dependence of the reaction rate on the temperature. The latter is supported by the lowest inclination of the curve (Fig. S4, A).

The turnover frequencies (TOFs) of acetaldehyde and ethyl acetate formation are listed in Table 5. The high activity of Cu/ZrO_2 catalysts in relation to ethyl acetate formation is supported by the higher values of the apparent $TOFs_{(N2O)}$, based on the Cu^0 surface area per gram of catalyst, compared to those found for Cu/SiO_2 catalyst [53]. The latter is more evident for Cu/*m*-ZrO_2 catalyst (Table 5). $TOFs_{(EXAFS)}$ show similar activities of acetaldehyde formation over all catalysts and the highest activity of ethyl acetate formation over Cu/*m*-ZrO_2.

Fig. 10 exhibits the evolution of the selectivity to propanone and ethyl acetate as a function of the reaction temperature at high contact time. It is observed that the selectivity to propanone for Cu/*am*-ZrO_2 and Cu/*m*-ZrO_2 catalysts increases at the expense of the decrease in the selectivity to ethyl acetate, which is much more visible for the second one at the highest reaction temperature.

The change in the amount of PCD and the water/PCD ratio for each catalyst at different reaction temperatures is shown in Fig. 11. The quantity of water increases in the following order: Cu/*am*-ZrO_2 < Cu/*m*-ZrO_2 < Cu/*t*-ZrO_2 (Table 4). Even though the highest amount of water and PCD as reaction effluent is observed for Cu/*t*-ZrO_2, the lowest water/PCD ratio is calculated. For Cu/*am*-ZrO_2 and Cu/*t*-ZrO_2 catalysts, practically, there is no significant change in the water/PCD ratio with the increase in reaction temperature (Fig. 11). It is interesting that the water/PCD ratio for Cu/*m*-ZrO_2 increases from 3.2 up to 5 at 498–523 K, and after that, it is decreased to 3.4 at the highest reaction temperature (548 K). The highest value of the ratio should be caused by the resulting amount of PCD formed upon a temperature increase, but the amounts of water do not follow the same trend (Fig. 11B). This phenomenon will be discussed in Section 4.2.

4. Discussion

4.1. Nature of the species in Cu/ZrO_2 system

The present results show that the zirconia-supported copper species in reduced catalysts are in different oxidation states, in the form of Cu^+ and Cu^0, which distribution depends on the nature of

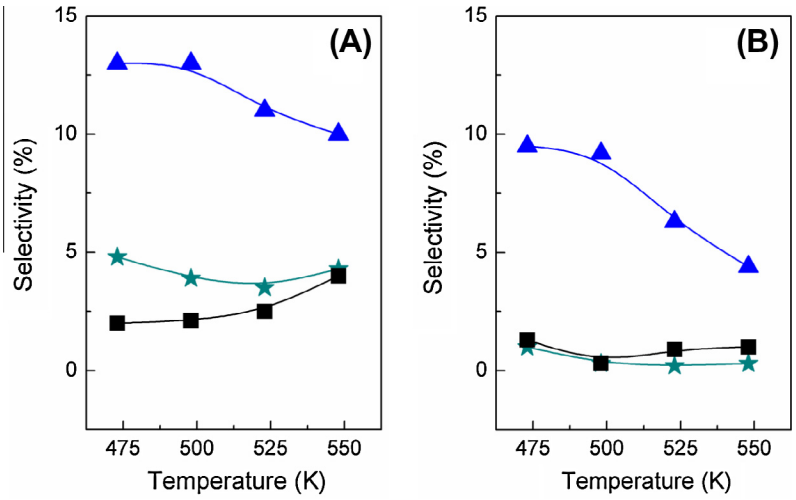

Fig. 8. Evolution of the selectivity to methyl ethyl ketone/buthanol (A) and crotonaldehyde (B) as a function of the reaction temperature for Cu/ZrO_2 catalysts: Cu/*am*-ZrO_2 (★); Cu/*m*-ZrO_2 (■) and Cu/*t*-ZrO_2 (▲).(W/F = 38 min, P_{EtOH} = 37.4 kPa).

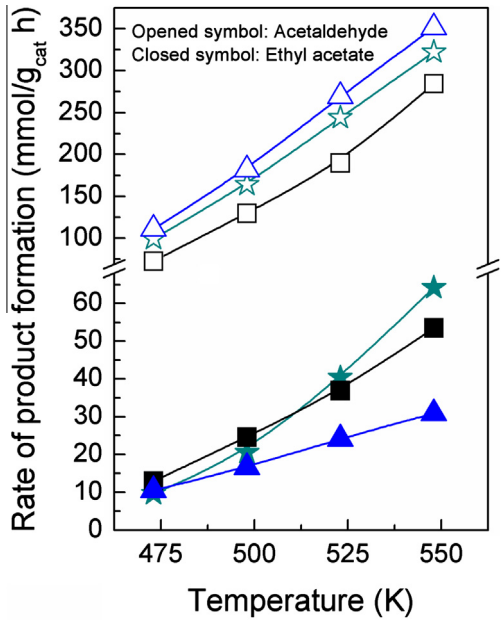

Fig. 9. Rate of the formation of acetaldehyde and ethyl acetate over Cu/ZrO_2 catalysts: Cu/*am*-ZrO_2 (★); Cu/*m*-ZrO_2 (■) and Cu/*t*-ZrO_2 (▲). (W/F = 1.2 min, P_{EtOH} = 37.4 kPa).

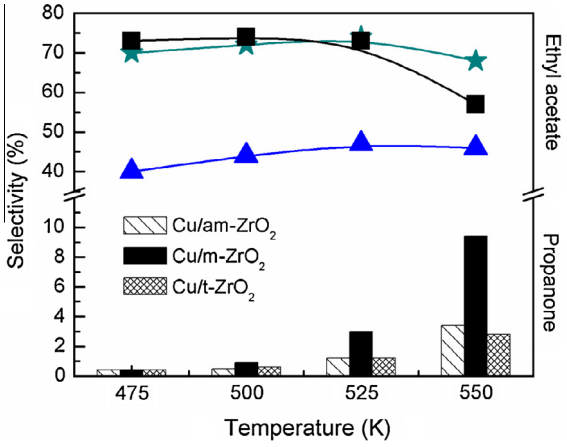

Fig. 10. Evolution of selectivity to ethyl acetate and propanone as a function of the reaction temperature for Cu/ZrO_2 catalysts: Cu/*am*-ZrO_2 (★); Cu/*m*-ZrO_2 (■) and Cu/*t*-ZrO_2 (▲). (W/F = 38 min, P_{EtOH} = 37.4 kPa).

ZrO_2 support phase. According to the literature data [54,55], the change in the proportion Cu^0/Cu^+ for copper samples supported on different zirconia phases can be attributed to several reasons that involve the following: (i) changes in the average Cu–Cu coordination number of Cu nanoparticle atoms owing to a high surface-to-volume ratio; (ii) increase in the electron density of supported particles in respect to bulk metal; (iii) bonding interactions at the interface and its nature; and (iv) differences in the polarization properties of the oxide substrates put in contact. Therefore, the changes in the electronic properties of copper have to be associated with one or more of these factors, which can be a function of the ZrO_2 kind. The observed equilibrium between Cu^+ and Cu^0 for the reduced Cu/*m*-ZrO_2 is a specific characteristic, which can explain in part the different behaviors of this catalyst in the reaction of ethanol conversion compared to Cu catalysts supported on *am*- and *t*-ZrO_2 phases.

Table 5
Apparent activation energy and pre-exponential factor of kinetics constant, turnover frequencies (TOF) for acetaldehyde and ethyl acetate formation. Reaction conditions for kinetic constant calculations: W/F = 1.2 min and P_{EtOH} = 37.4 kPa. Reaction conditions for TOF calculations: W/F = 1.2 min, P_{EtOH} = 37.4 kPa, T_{reac} = 473 K.

Catalysts	Apparent E_a (kJ/mol)		$TOF_{(N2O)}$ (s^{-1})		$TOF_{(EXAFS)}$ (s^{-1})	
	AcH	EtOAc	AcH ($\times 10^4$)	EtOAc ($\times 10^4$)	AcH ($\times 10^4$)	EtOAc ($\times 10^4$)
Cu/*am*-ZrO_2	33.9 (±0.3)	54.9 (±0.2)	810	78	217	21
Cu/*m*-ZrO_2	38.5 (±1.1)	40.3 (±1.4)	640	114	222	40
Cu/*t*-ZrO_2	36.3 (±4.6)	30.8 (±3.3)	580	55	217	21
Cu/SiO_2-Aq	37.5	–	410 [59]	3.9 [59]	–	–
CuSiO_2-IE	42.5	–	1930 [59]	26.0 [59]	–	–

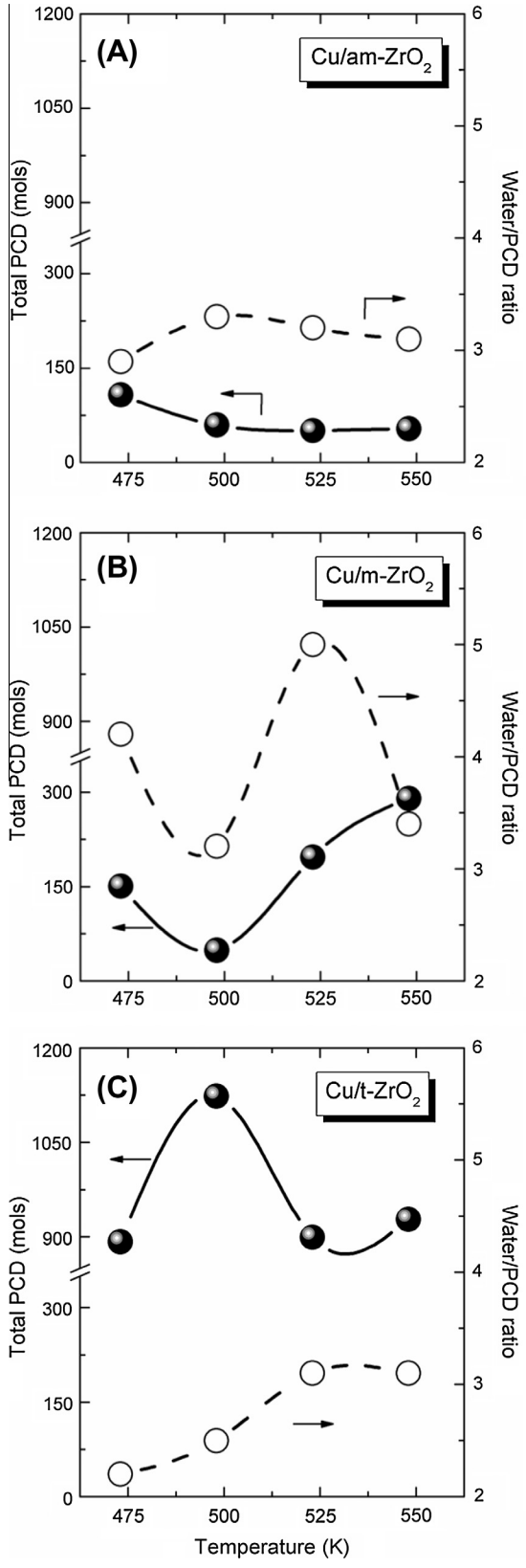

Fig. 11. Effect of the reaction temperature on the change in total PCD and ratio of water/PCD for (A) Cu/*am*-ZrO_2, (B) Cu/*m*-ZrO_2, (C) Cu/*t*-ZrO_2. (W/F = 38 min, P_{EtOH} = 37.4 kPa).

For zirconia-supported Cu samples, the interfaces between Cu and ZrO_2 could be different in respect to copper particle size and copper oxide support contact structure. The presence of defects on the oxide surface of ZrO_2 revealed by the presence of oxygen anions and/or oxygen vacancies might provide sites for nucleation and growth of metal copper particles. For example, it was found by measuring the number density of oxygen vacancies and gold particles that the density of oxygen vacancies on TiO_2 (110) decreases during gold particle growth [56]. The theoretical results showed that the adsorption energy of a single gold atom on an oxygen vacancy site is more stable by 0.45 eV than on the stoichiometric surface [56].

The formation of different Cu^0/Cu^+ ratios for Cu/ZrO_2 samples might be related to a strong interaction of the copper particles with the matrix. According to some authors [22], the presence of Cu^+ species on the surface of supported Cu catalysts is associated with the dispersion degree of supported phase. They showed that the increase in copper dispersion degree leads to an increase in the energy of Cu interaction as well as to a decrease in the value of the Auger parameter, α_{Cu}. Concerning the XPS results listed in Table 2, the change in α_{Cu} is in the following order: Cu/*t*-ZrO_2 > Cu/*m*-ZrO_2 > Cu/*am*-ZrO_2. Therefore, the lowest α_{Cu} value is detected for copper species supported on *am*-ZrO_2 (1848.2 eV), to which corresponds the highest BE value of Cu $2p_{3/2}$ (932.9 eV). The shift of the valence band to a higher binding energy is a result of the reduced particle size [57]. The small particles or isolated Cu atoms at the interface between metal and oxide support become electropositive charged, caused by the electron charge transfer from the metal to support [57]. The IR of CO adsorption data (Fig. 6) show that the Cu^+ species are dominant over *am*-ZrO_2 surface. The presence of Cu^+ as dominant species is also supported by the low value of the metallic copper surface area over *am*-ZrO_2, revealed by the N_2O titration (Table 1). It should be noted that the well-dispersed copper oxide species is not easily reduced to metal due to the presence of oxygen vacancy in ZrO_2, which protects the interfacial Cu^+ from further reduction during catalytic reaction [58]. It can be concluded that well-dispersed copper species present in reduced Cu/*am*-ZrO_2. The lowest value of XPS atomic Cu/Zr ratio for Cu/*am*-ZrO_2 (Table 2) should be related to a high amount of exposed Zr atoms under XPS measurements, due to the highest specific surface area of support.

It was concluded [22] that ZrO_2 support strongly stabilizes the Cu^+ state because these species can be obtained just by annealing under ultrahigh vacuum, while a reduction treatment (H_2 at 523 K) is necessary for the case of SiO_2-supported samples, due to the difference in the overall polarization property of the both oxides; the covalence of Cu–O–Me bond was higher when copper oxide is deposited over silica. Interactions with an oxide support can accelerate or decrease the rate of CuO reduction [59]. Quantitative analysis of the variations between the well-dispersed phases and bulk materials has been done by comparing the changes with quantum mechanical calculations of the Cu–O–Me bond structure at the interface in terms of covalence, density of charge distribution, etc. [60]. The interface between Cu and Cu_2O was investigated by means of density functional theory (DFT), and it was shown that a continuous chemical bonding across the Cu–Cu_2O system exists [61].

It is evident from the EXAFS analysis (Table 3) that the zirconia-supported copper nanoparticles behave very differently from their bulk forms, due to the electronic and structural effects of materials. On the surface of copper, it is difficult to avoid the perturbation of oxygen from the OH groups as well as from the bulk ZrO_2, even if the catalyst was reduced at high temperature. Copper has a completely filled 3d band at the Fermi level; however, the smaller Cu particles in a strong interaction with the support surface might have a partially filled 3d band with a high density of states at Fermi level, thereby resulting in a lower electron density. The variation in the inter-atomic distances, R_{Cu-Cu} and R_{Cu-O}, indicates different interactions between the copper atoms and between copper and

oxygen atoms, respectively (Table 3). This is well visible for Cu species supported on *am*- and *t*-zirconia, which have smaller nanocluster size (4.4 and 2.9 nm for Cu/*am*-ZrO_2 and Cu/*t*-ZrO_2, respectively, Table 3) compared to that for Cu/*m*-ZrO_2 (8.7 nm). In addition, the presence of oxygen causes a stretching in the Cu–Cu distance from 2.54 to 3.03 Å for bulk Cu^0 and Cu_2O, respectively. The values of R_{Cu-Cu} for Cu/*am*-ZrO_2 and Cu/*t*-ZrO_2 related to the Cu_2O contribution are 2.67 and 2.70 ± 0.002 Å, values which are shorten compared to that of the bulk Cu_2O (3.03 ± 0.004 Å). Thus, geometrically, it is inferred that the oxygen species linked to copper nanoclusters in Cu/*am*-ZrO_2 and Cu/*t*-ZrO_2 is more exposed, being seen in Fig. S5. This kind of oxygen will be called by us "label" oxygen.

The "label" oxygen weakly linked to the copper nanoparticles would be readily decomposed on the surface of Cu/*t*-ZrO_2 system under high vacuum treatment (10^{-10} Torr), since during the XPS measurements, metallic copper was detected only (Table 2). This could be caused by some photoreduction in copper oxide species irradiated by X-ray and under vacuum. On the other hand, concerning the EXAFS analysis, the electron transition of 1s → (4pz + L) at K Cu-edge typical for bulk Cu_2O reference is not detected for Cu/*t*-ZrO_2; copper oxide species is totally reduced to metallic copper (Fig. S1). It should be noted that the photon energy over the samples during XAS experiments was much higher (9000 eV) than that during the XPS measurements (about 1000 eV). Probably, there is no real ionic interaction between the oxygen and copper, due to the weakly bonded oxygen to copper surface. The same consideration is observed for Cu/*am*-ZrO_2 and Cu/*m*-ZrO_2, but the copper oxide species (Cu^+) is much more stable on *am*-ZrO_2 and *m*-ZrO_2 compared to that on *t*-ZrO_2.

Even though many studies, especially theoretical studies, have been suggested that the copper oxide support interface plays a significant role for the creation of oxygen sites, one question arises how the limited surface area of the copper catalytic system, like Cu/*m*-ZrO_2 catalyst with the highest particle size (8.7 nm), can be responsible for the creation of oxygen species, being revealed by the presence of stable Cu^+ species under reduction up to 800 K. Caballero et al. [23] also reported evidence of high stability of Cu^+ oxide phase on ZrO_2 support based on in situ Cu K-edge XANES measurements under reaction conditions. Sloczynski et al. [34] found that the reduction in CuO is an autocatalytic consecutive reaction, and the intermediate product is amorphous Cu_2O.

The slowly transition of CuO to Cu^0 and the high stability of Cu^+ species for Cu/*m*-ZrO_2 during the XANES-TPR analysis (Fig. 5) should be correlated with the strong interaction of the copper surface with oxygen species deposited at the metal-support interface, as well as on the copper particles. This is in accordance with the observations by Knapp et al. [45]. The authors reported that the formation of oxide species can occur on the surface of copper nanoparticles, as well as at the interface between Cu and oxide support. The oxygen atoms are located to a large extent on the accessible surface of the copper metal particles, since the fraction of the potential interface between the agglomerated metal particles and the oxide support is much smaller than the fraction of the oxidized Cu [45].

The surface oxygen species (O_s) might be formed by different ways in Cu/ZrO_2 system, especially under reaction conditions, which will be discussed in detail in Section 4.2. It should be noted that the oxygen species on the copper particles in Cu/*m*-ZrO_2 is caused by the oxygen transfer from *m*-ZrO_2 substrate to copper surface, due to the high oxygen-rich interface generated by spillover mechanism between the copper and the zirconia during the reduction process. The high concentration of oxygen anions, characterizing the *m*-ZrO_2 surface, is revealed by the FTIR of CO adsorption (Fig. 6E). This is similar to the observation for TiO_2-supported Cu [62], where it was suggested that the oxygen migration to the Cu surface may occur only when a significant fraction of the titania surface in Cu/TiO_2 system is still exposed. This suggests that the role of *m*-ZrO_2 support in the Cu/*m*-ZrO_2 system is to provide an extra charge to copper particles or oxygen to proximity of Cu. This interpretation implies that relatively large metal Cu particles in Cu/*m*-ZrO_2 system distinguish themselves from smaller ones by the presence of surface adatoms, which are quite stable even upon hydrogen reduction up to 800 K [63].

The decreased value of the coordination number of Cu–Cu atoms (Table 3) and the low temperature reduction in copper species on *t*-ZrO_2 (Figs. 3 and 5) consist with the increase in electron density of the Cu atoms in very small metal particles, which are dominant on the support surface (Table 2). In general, it is expected that the fraction of oxygen over small metallic Cu particles is higher compared to that on bigger ones [45]. For Cu/*am*-ZrO_2 sample, where the Cu^+ species is dominant, it can be concluded that a great part of the copper species is in interaction with the oxygen sites originated from the oxygen-rich interface at Cu/*am*-ZrO_2 by oxygen diffusion, similar to that observed for Cu/*m*-ZrO_2. In opposite to that, a small fraction of the copper species should be covered by oxygen in Cu/*t*-ZrO_2, i.e., the positive charged copper species is mainly caused by the direct connection with the support surface. The higher stability of CO desorbed up to a higher temperature on Cu/*t*-ZrO_2 compared to that on Cu/*m*-ZrO_2 would be related to a covalence character of the Cu–O–Zr interaction due to the different polarities of both zirconia phases.

Considering that the oxygen is highly negatively charged, it is reasonable from electrostatic interaction that the higher the cationic charge on Cu is, the stronger the bonding ability to the O atom will be. However, theoretical studies have shown [64] that the adsorption energy of oxygen for Cu/ZrO_2 (2.25 eV) is higher compared to those for Cu(1 1 1) (1.44 eV) or *cus* Cu (0.87 eV). This implies that the location of adsorbed O prefers a high coordination environment on neutral Cu system where the surface electron density is high, in line with the strong ionic bonding character of O and Cu. Studying the interface between Cu and Cu_2O by DFT [61], it was shown that a continuous chemical bonding exists across the Cu–Cu_2O system, i.e., the copper atoms are simultaneously connected by a metallic bonding with the copper atoms in both the metal and the oxide phase, and besides, they form ionic-covalent connections with the oxygen.

4.2. Relation between the copper species, acid–base properties and catalytic performance of Cu/ZrO_2 catalysts

The results of catalytic test of ethanol reaction conclude that the product distribution is strongly influenced by the structure and electronic properties of the particles and the surface acid–base properties of the catalysts as a function of the kind of ZrO_2 phase. Additionally, ethanol reaction gives an opportunity to obtain information about the electronic properties of Cu/ZrO_2 catalysts.

It is well known that ethanol is converted via four main groups of reaction; dehydrogenation, dehydrogenation coupling, dehydration, and hydrogenolysis. Dehydrogenation of ethanol forms acetaldehyde as a primary product. The consecutive aldol condensation of acetaldehyde yields *n*-butanol, crotonaldehyde, and ketones. Dehydration reaction leads to formation of diethyl ether and ethylene. It was reported [65] that the strong acidic sites are responsible for the dehydration reaction, whereas dehydrogenation requires metallic, moderate acid sites, and strong basic sites.

The surface and acid–base properties derived from the XPS analysis and DRIFTS of CO adsorption show appreciable information about the surface anionic defects associated with the creation of $Zr^{\delta+}$ species on the surface of reduced materials. Three different types of basic sites are detected over the surface of ZrO_2-supported copper catalysts: strongly basic surface O^{2-} ions, medium-strength

Zr^{4+}–O^{2-} pairs, and low-strength OH groups. Their relative concentration or density depends on the kind of ZrO_2 phase. The bridged-bonded OH groups for *am*- and *m*-ZrO_2 phases can be easily decomposed under increasing the reaction temperature, and more oxygen anions and/or oxygen vacancies are formed, whereas, *cus* $Zr^{\delta+}$ and Zr^{4+} cations attributed to strong acid sites of Lewis type are stabilized for Cu/*t*-ZrO_2.

The high rate of acetaldehyde formation for Cu/*t*-ZrO_2 catalyst (Fig. 9) can be related to the presence of "label" oxygen on the well-dispersed metallic copper nanoparticles, which facilitates the formation of ethoxide intermediate via O–H scission in ethanol. It was shown that the presence of oxygen facilitates the catalyst dehydrogenation activity [63]. Similar to methanol activation on oxidized single-crystal Cu surfaces [66], the reactivity of ethanol to acetaldehyde can be greatly enhanced on the oxygen covered copper clusters, because the O–H bond scission is facilitated by the adsorbed oxygen. Surface science studies have shown that the co-adsorbed oxygen on the surface of transition metals act as a Brönsted base to facilitate the O–H bond cleavage [63]. Subsequent C–H bond cleavage leads to the formation of acetaldehyde. This step can be also catalyzed by the presence of surface oxygen. The surface ethoxide intermediate can either loss hydrogen to produce acetaldehyde or pick up hydrogen to form ethanol and then decomposes to acetaldehyde. The dependence of the rate of alcohol dehydrogenation on the oxygen coverage may be interpreted in terms of Langmuir type dependence on the oxygen surface coverage [67].

The catalytic performance of Cu/*t*-ZrO_2 is also determined by the presence of strong Lewis acid sites (Zr^{4+}) and by the low basic sites density defined by the dominant Cu^0. The β-aldolization of acetaldehyde is strongly promoted, since the aldolization reaction requires basic sites to abstract α-hydrogen atom and strong Lewis acid sites to bind the two molecules of acetaldehyde [68]. Acetaldehyde condensation toward *n*-butanol and crotonaldehyde is a bimolecular reaction between adjacent adsorbed acetaldehyde species that requires acid–base pair sites [58], which is a characteristic of *t*-ZrO_2 surface.

For Cu/*t*-ZrO_2 catalyst, the selectivity to methyl ethyl ketone and crotonaldehyde decreases with increasing the reaction temperature at high contact time (Fig. 8). In general, the aldolization process is accompanied by a high amount of water released under reaction conditions (Table 4). The remarkably amounts of PCD for Cu/*t*-ZrO_2 do not correspond to the respective amounts of released water. Cu/*t*-ZrO_2 catalyst is characterized by lower water/PCD ratios compared to those for Cu/*am*-ZrO_2 and Cu/*m*-ZrO_2 (Fig. 11). This suggests some regeneration of the oxygen sites by consumption of the hydroxyls of *t*-ZrO_2 under reaction, similar to the observations in Ref. [69].

The surface oxygen linked to copper nanoclusters in Cu/*am*-ZrO_2 affects strongly the electron density of copper species. The dominant Cu^+ species and the low basic sites density determined by the low strength of OH groups of *am*-ZrO_2 seem to be responsible for the high selectivity to acetaldehyde (Table 4, Fig. 7B and C). It has been shown [70] that isolated copper ions catalyze the dehydrogenation of ethanol to acetaldehyde formation, while multiple Cu ensembles show high yields of ethyl acetate. The absence of strong Lewis acid sites does not provoke the strong acetaldehyde condensation similar to that observed for Cu/*t*-ZrO_2. Increasing the temperature of reaction, probably, causes a thermal decomposition of the hydroxyls at *am*-ZrO_2 that leads to the formation of more oxygen anions or oxygen vacancies and to the change in the electron density of copper species caused by the oxygen migration. The last provokes the ethyl acetate formation, being revealed by the increase in the rate of ethyl acetate formation at temperature $\geqslant$525 K (Figs. 7B and 9), as well as by the lower apparent activation energy value in Table 5. On the other hand, depending on the oxygen resistance on the copper surface, its consumption by ethanol leads to the increase in acetaldehyde formation (Table 4 and Fig. 9).

It was suggested by Inui et al. [4,5] that the coupling of aldehyde with alcohol or ethoxide species for ethyl acetate formation occurs over the mixed metal oxides surface not over the Cu metal surface in Cu catalysts supported on Zn–Zr–Al–O system. The dehydrogenated ethanol or the acetaldehyde was adsorbed on the acid sites, while the hydrogen of the OH group in ethanol was abstracted by the surface base sites forming surface ethoxide [4,5]. Then, a hemiacetal between these products is formed, which dehydrogenates very fast and produces ethyl acetate. It means that more active sites, like Cu^0 and Cu^+, will accelerate the acetal adsorption.

The relatively invariable value of the water/PCD ratio for Cu/*am*-ZrO_2 suggests that the consumed hydroxyls in the processes of acetaldehyde condensation and ethanol dehydration are in equilibrium with the regeneration of OH sites and/or oxygen sites of *am*-ZrO_2 at all reaction temperatures. It can be concluded that the oxygen species at ZrO_2 tunes the electron density of Cu species on the surface of *am*-ZrO_2.

As was mentioned above, a great part of the copper surface in Cu/*m*-ZrO_2 is in interaction with the oxygen being revealed by the high stability of Cu^+ species, which are in some equilibrium with Cu^0. The presence of Cu species with different electron densities and the high concentration of basic sites (O^{2-}) defined by DRIFTS are responsible for the high selectivity to ethyl acetate of Cu/*m*-ZrO_2. TOFs of ethyl acetate formation highlight that the active copper species over Cu/*m*-ZrO_2 catalyst differs from copper species of Cu/*t*-ZrO_2 and Cu/*am*-ZrO_2 (Table 5).

It should be noted that the lowest apparent rate of acetaldehyde formation for Cu/*m*-ZrO_2 catalyst at short contact time (Table 5 and Fig. 9) could be masked by its fast consumption for ethyl acetate formation. In reality, the acetaldehyde takes part in the formation of ethyl acetate formation, which means that its participation in the reaction could be revealed by spillover and coupling reaction between the ethoxide and acyl adsorbates. The acetaldehyde co-feed with ethanol leads to the formation of products of aldol condensation [4,71], suggesting that the ethyl acetate reaction proceeds via Langmuir–Hinshelwood mechanism [72]. The diffusion rate of adsorbed acetaldehyde should be determined by the electronic properties of copper nanoclusters in interface with *m*-ZrO_2.

The Cu catalysts supported on *am*- and *t*-ZrO_2 exhibit a relatively high stability of the selectivity to ethyl acetate formation at all reaction temperatures. A certain decrease in the ethyl acetate formation at temperature above 513 K is observed for Cu/*m*-ZrO_2 catalyst at high contact time (Figs. 7B and 10). The latter is accompanied with a strong increase in the selectivity to propanone formation on Cu/*m*-ZrO at 525–550 K, being is seen Fig. 10. The relationship between the propanone formation and the loss of ethyl acetate selectivity of Cu/*m*-ZrO_2 seems to indicate that oxygen mobility may be involved in the performance of the catalyst.

It was shown [73] that CuO/CeO_2 exhibits a high capacity for propanone formation in the ethanol reaction, where ceria is an oxygen supplier due to its high oxygen storage capacity. However, the present reaction over Cu/ZrO_2 occurs in non-oxidative conditions employing anhydrous ethanol as reactant and in reductive atmosphere. Similar to CeO_2, bulk *m*-ZrO_2 is also characterized by oxygen-rich surface. The increase in the reaction temperature above 513 K could cause a loss of the oxygen from the bulk *m*-ZrO_2, leading to a change in the electron density of surface copper species active for ethyl acetate formation. Propanone can be formed by an oxidation of acetaldol with the surface oxygen (O_s) adsorbed on Cu/ZnO/Al_2O_3 catalyst [74]. The oxygen consumed during the acetaldol oxidation could be regenerated by the water decomposition: $H_2O \rightarrow H_2 + O_s$ or by the CO_2 dissociation, pro-

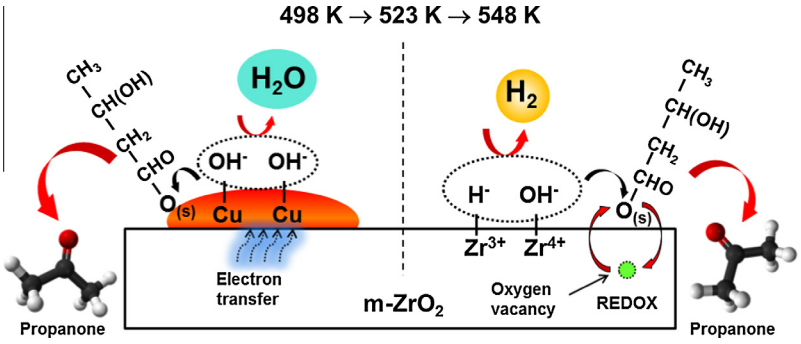

Fig. 12. Schematic illustration of the proposed mechanisms for the formation of atomic oxygen on the surface of copper and of m-ZrO_2.

duced during propanone formation: $CO_2 \rightarrow CO + O_s$ [74]. However, according to Nakamura et al. [75], the possibility for CO_2 dissociation on the surface of Cu(1 1 0) under the present reaction conditions should be very small. Also, the direct dissociation of H_2O is kinetically rather difficult at the Cu sites. A coupling of OH groups by proton-transfer channel according to Henderson [76] could be predominantly responsible for the surface oxygen formation on Cu/m-ZrO_2 catalyst: $2OH^* \rightarrow O^* + H_2O^*$ (Fig. 12). DFT studies of copper surface also showed that the disproportion of OH groups is a preferable way for the water dissociation [64].

The slight decrease in ethyl acetate formation for Cu/m-ZrO_2 at temperature range 498–523 K is accompanied with a strong increase in the water/PCD ratio from 3.2 to 5 independent of the increase in the products of the aldol condensation and ethanol dehydration (Figs. 10 and 11B). Probably, the coupling mechanism of OH groups on the copper surface at that temperature range is responsible for the formation of water and adsorbed oxygen on Cu/m-ZrO_2, as well as for the enhanced propanone formation. The readily consumption of the oxygen for ethyl acetate and propanone formation would cause a loss of the electron transfer from the bulk m-ZrO_2 justifying the ethyl acetate selectivity decrease. The subsequently increase in the reaction temperature from 523 up to 548 K leads to a decrease in the water/PCD ratio value from 5 to 3, as well as of ethyl acetate formation, which suggests that other mechanism is involved in the formation of adsorbed oxygen. In this case, the surface oxygen can be formed by the interaction of the hydroxyls, near Zr^{4+} cations, with a hydrogen anion at *cus* Zr^{3+} [77], acting as a Lewis base: $OH^- + H^- \rightarrow H_2\uparrow + O^{2-}$ (Fig. 12). This leads to the increase in propanone formation, since acetaldol also reacts with the oxygen generated by this mechanism on the support surface. In Fig. 12, it is attempted to illustrate the proposed mechanism for the formation of oxygen on the surface of Cu nanoparticles and of m-ZrO_2 under ethanol reaction at reaction temperature range of 498–548 K.

It should be noted that the catalysts showed high ethanol conversion stability during 12 h of work at all reaction temperatures (Fig. S6). It can be summarized that *am*- and m-ZrO_2 phases are suitable carriers for supported Cu catalysts for ethyl acetate formation.

5. Conclusions

Copper catalysts supported on different ZrO_2 polymorphs are found to be active catalysts for ethanol dehydrogenation to acetaldehyde or ethyl acetate depending on the kind of zirconia phase. The catalytic properties of Cu catalyst supported on *am*-, *m*-, or *t*-ZrO_2 phase are due the specific electron density of supported copper species (Cu^0 and Cu^+) defined by the particle size and the interface at copper metal oxide support. The active surface sites for Cu/m-ZrO_2 catalyst show that the higher rate of ethyl acetate formation is determined by the high oxygen mobility from the bulk m-ZrO_2 phase to copper species causing a high density of basic sites and a more heterogeneous distribution of the surface copper species (Cu^0/Cu^+). The increase in reaction temperature at short contact time of 1.2 min leads to the increase in the rate of ethyl acetate formation over Cu/*am*-ZrO_2 catalyst, provoked by the oxygen transfer from Cu to bulk *am*-ZrO_2 and establishment of oxygen vacancies, which subsequently are diffused to copper species by redox mechanism. The last one provokes the highest rate of ethyl acetate formation over Cu/*am*-ZrO_2 at reaction temperature $\geqslant$525 K. The high density of Lewis acid sites defined by *cus* Zr^{4+} centers and the predominance of superficial Cu^0 species over *t*-ZrO_2 leads to the formation of by-products by aldol condensation.

Acknowledgments

The authors gratefully acknowledge by support finance for this research from CNPq and FAPESP and the Brazilian Synchrotron Light Laboratory (LNLS) for the XAS beamline experiments (D06A-DXAS 10156) and (D04B-XAFS1). S.D. is gratefully acknowledged to Bulgarian Ministry of Education, Science and Youth (Project DTK-02/36).

Appendix A. Supplementary material

Supplementary data associated with this article can be found, in the online version, at http://dx.doi.org/10.1016/j.jcat.2013.06.022.

References

[1] V.D. Bastos, Etanol Alcoholquimica e biorrefinarias, BNDES Set. 25 (2007) 5–38.
[2] P. Chladek, E. Croiset, W. Epling, R.R. Hudgins, Can. J. Chem. Eng. 85 (2007) 917–924.
[3] A.B. Sánchez, N. Homs, J.L.G. Fierro, P.R.d. La-Piscina, Catal. Today 107–108 (2005) 431–435.
[4] K. Inui, T. Kurabayashi, S. Sato, N. Ichikawa, J. Mol. Catal. A: Chem. 216 (2004) 147–156.
[5] K. Inui, T. Kurabayashi, S. Sato, Appl. Catal. A: Gen. 237 (2002) 53–61.
[6] S.W. Colley, J. Tabatabaei, K.C. Waugh, M.A. Wood, J. Catal. 236 (2005) 21–33.
[7] A.B. Gaspar, A.M.L. Esteves, F.M.T. Mendes, F.G. Barbosa, L.G. Appel, Appl. Catal. A: Gen. 363 (2009) 109–114.
[8] L. Wang, W. Zhu, D. Zheng, X. Yu, J. Cui, M. Jia, W. Zhang, Z. Wang, Reac. Kinet. Mech. Catal. 101 (2010) 365–375.
[9] N. Iwasa, N. Takezawa, Bull. Chem. Soc. Jpn. 64 (1991) 2619–2623.
[10] J. Agrell, H. Birgersson, M. Boutonnet, I. Melián-Cabrera, R.M. Navarro, J.L.G. Fierro, J. Catal. 219 (2003) 389–403.
[11] M. Shimokawabe, H. Asakawa, N. Takezawa, Appl. Catal. 59 (1990) 45–58.
[12] F.W. Chen, H.C. Yang, L.S. Roselin, W.Y. Kuo, Appl. Catal. A: Gen. 304 (2006) 30–39.
[13] K.T. Jung, A.T. Bell, Catal. Lett. 80 (2002) 63–68.
[14] M.D. Rhodes, A.T. Bell, J. Catal. 233 (2005) 198–209.
[15] R.A. Koeppel, A. Baiker, A. Wokaun, Appl. Catal. A: Gen. 84 (1992) 77–102.
[16] X.R. Zhang, L.C. Wang, C.Z. Yao, Y. Cao, W.L. Dai, H.Y. He, K.N. Fan, Catal. Lett. 102 (2005) 183–190.
[17] K. Takeshita, S. Nakamura, K. Kawamoto, Bull. Chem. Soc. Jpn. 51 (1978) 2622–2627.

[18] A.B. Gaspar, F.G. Barbosa, S. Letichevsky, L.G. Appel, Appl. Catal. A: Gen. 380 (2010) 113–117.
[19] H. Oguchi, H. Kanai, K. Utani, Y. Matsumura, S. Imamura, Appl. Catal. A: Gen. 293 (2005) 64–70.
[20] I. Ritzkopf, S. Vukojevic, C. Weidenthaler, J.-D. Grunwaldt, F. Schüth, Appl. Catal. A: Gen. 302 (2006) 215–223.
[21] G. Águila, S. Guerrero, P. Araya, Catal. Commun. 9 (2008) 2550–2554.
[22] J.P. Espinós, J. Morales, A. Barranco, A. Caballero, J.P. Holgado, A.R. González-Elipe, J. Phys. Chem. B 106 (2002) 6921–6929.
[23] A. Caballero, J.J. Morales, A.M. Cordon, J.P. Holgado, J.P. Espinos, A.R. Gonzalez-Elipe, J. Catal. 235 (2005) 295–301.
[24] G.K. Chuah, S.H. Liu, S. Jaenicke, J. Li, Microporous Mesoporous Mater. 39 (2000) 381–392.
[25] K.J. Soerensen, N.W. Cant, Catal. Lett. 33 (1995) 117–125.
[26] Y. Okamoto, H. Gotoh, H. Aritani, T. Tanaka, S. Yoshida, J. Chem. Soc., Faraday Trans. 93 (1997) 3879–3885.
[27] A. Frenkel, Z. Krystallogr. 222 (2007) 605–611.
[28] S. Ardizzone, C.L. Bianchi, J. Electroanal. Chem. 465 (1999) 136–141.
[29] S. Velu, K. Suzuki, C.S. Gopinath, H. Yoshida, T. Hattori, Phys. Chem. Chem. Phys. 4 (2002) 1990–1999.
[30] S. Ardizzone, C.L. Bianchi, Surf. Interf. Anal. 30 (2000) 77–80.
[31] M.K. Dongare, A.M. Dongare, V.B. Tare, E. Kemniz, Solid State Ionics 455 (2002) 152–153.
[32] J.A. Navio, M.C. Hidalgo, G. Colon, S.G. Botta, M.I. Letter, Langmuir 17 (2001) 202–210.
[33] C. Morant, J.M. Sanz, L. Galan, L. Soriano, F. Rueda, Surf. Sci. 218 (1989) 331–345.
[34] J. Sloczynski, R. Grabowski, A. Kozlowska, P.K. Olszewski, J. Phys. Chem. Chem. Phys. 5 (2003) 4631–4640.
[35] C.Z. Yao, L.C. Wang, Y.M. Liu, G.S. Wu, Y. Cao, W.L. Dai, H.Y. He, K.N. Fan, Appl. Catal. A: Gen. 297 (2006) 151–158.
[36] K. Shimizu, H. Maeshima, H. Yoshida, A. Satsuma, T. Hattori, Phys. Chem. Chem. Phys. 3 (2001) 862–866.
[37] D.M. Pickup, I. Ahmed, V. FitzGerald, R.M. Moss, K.M. Wetherall, J.C. Knowles, M.E. Smith, R.J. Newport, J. Non-Cryst. Solids 352 (2006) 3080–3087.
[38] L.S. Kau, D.J. Spira-Solomon, J.E. Penner-Hahn, K.O. Hodgson, E.I. Solomon, J. Am. Chem. Soc. 109 (1987) 6433–6442.
[39] M.H. Groothaert, J.A. van Bokhoven, A.A. Battiston, B.M. Weckhuysen, R.A. Schoonheydt, J. Am. Chem. Soc. 125 (2003) 7629–7640.
[40] L.A. Grunes, Phys. Rev. B 27 (1983) 2111–2131.
[41] Q. Wang, J.C. Hanson, A.I. Frenkel, J. Chem. Phys. 129 (2008) 234502–234507.
[42] Y. Okamoto, T. Kubota, H. Gotoh, Y. Ohto, H. Aritani, T. Tanaka, S. Yoshida, J. Chem. Soc., Faraday Trans. 94 (1998) 3743–3752.
[43] F. Yang, Y. Choi, P. Liu, J. Hrbek, J.A. Rodriguez, J. Phys. Chem. C 114 (2010) 17042–17050.
[44] J. Engeldinger, C. Domke, M. Richter, U. Bentrup, Appl. Catal. A: Gen. 382 (2010) 303–311.
[45] R. Knapp, S.A. Wyrzgol, A. Jentys, J.A. Lercher, J. Catal. 276 (2010) 280–291.
[46] A. Dandekar, M.A. Vannice, J. Catal. 178 (1998) 621–639.
[47] D.F. Cox, K.H. Schulz, Surf. Sci. 249 (1991) 138–148.
[48] D. Bianchi, T. Chafik, M. Khalfallah, S.J. Teichner, Appl. Catal. A: Gen. 112 (1994) 57–73.
[49] K.T. Jung, A.T. Bell, J. Mol. Catal. 163 (2000) 27–42.
[50] G. Cerrato, S. Bordiga, S. Barbera, C. Morterra, Surf. Sci. 377–379 (1997) 50–55.
[51] K. Pokrovsky, K.T. Jung, A.T. Bell, Langmuir 17 (2001) 4297–4303.
[52] B. Bachiller-Baeza, I. Rodrigues-Ramo, A. Guerrero-Ruiz, Langmuir 14 (1998) 3556–3564.
[53] B.A. Raich, H.C. Fohy, Ind. Eng. Chem. Res. 37 (1998) 3888–3895.
[54] A. Barranco, F. Yubero, J.A. Mejias, J.P. Espinos, A.R. Gonzalez-Elipe, Surf. Sci. 482–485 (2001) 680–686.
[55] J.A. Mejias, V.M. Jimenez, G. Lassaleta, A. Fernandez, J.P. Espinos, A.R. Gonzalez-Elipe, J. Phys. Chem. 100 (1996) 16255–16262.
[56] E. Wahlstrom, N. Lopez, R. Schaub, P. Thostrup, A. Ronnau, C. Africh, E. Laegsgaard, J.K. Norskov, F. Besenbacher, Phys. Rev. Lett. 90 (2003) 026101–026104.
[57] M. Rønning, F. Huber, H. Meland, H. Venvik, D. Chen, A. Holmen, Catal. Today 100 (2005) 249–254.
[58] W.P. Dow, T.J. Huang, J. Catal. 160 (1996) 171–182.
[59] J.A. Rodriguez, J.Y. Kim, J.C. Hanson, M. Pérez, A.I. Frenkel, Catal. Lett. 85 (2003) 247–254.
[60] W. Grüner, N.W. Hayes, R.W. Joyner, E.S. Shpiro, H. Rafiq, M. Siddiqui, G.N. Baeva, J. Phys. Chem. 98 (1994) 10832–10846.
[61] O.L. Blajiev, A. Hubin, Electrochim. Acta 50 (2005) 4297–4307.
[62] K. Varazo, F.W. Parsons, S. Ma, D.A. Chen, J. Phys. Chem. B 108 (2004) 18274–18283.
[63] K.Y. Guan, E.J.M. Hensen, Appl. Catal. A: Gen. 361 (2009) 49–56.
[64] Q.L. Tang, Z.P. Liu, J. Phys. Chem. C 114 (2010) 8423–8430.
[65] M.E. Manriquez, T. Lopez, R. Gomez, J. Navarrete, J. Mol. Catal. A: Gen. 220 (2004) 229–237.
[66] J.N. Russel, S.M. Gates, J.T. Yates, Surf. Sci. 163 (1985) 516–540.
[67] B.A. Sexton, A.E. Hughes, N.R. Avery, Surf. Sci. 155 (1985) 366–386.
[68] A. Yee, S.J. Morrison, H. Idriss, Catal. Today 63 (2000) 327–335.
[69] K.G. Azamm, I.V. Babich, K. Seshan, L. Lefferts, J. Catal. 251 (2007) 153–162.
[70] J.L. Gole, M.G. White, J. Catal. 204 (2001) 249–252.
[71] A.G. Sato, P. Diogo Volanti, I.C. de Freitas, E. Longo, J.M.C. Bueno, Catal. Commun. 26 (2012) 122–126.
[72] I. Chorkendorff, J.W. Niemantsverdriet, Concepts of Modern Catalysis and Kinetics, Copyright _ 2003 WILEY-VCH Verlag GmbH & Co. KGaA, Weinheim, p. 452, ISBN: 3-527-30574-2.
[73] T. Nishiguchi, T. Matsumoto, H. Kanai, K. Utani, Y. Matsumura, W.J. Shen, S. Imamura, Appl. Catal. A: Gen. 279 (2005) 273–277.
[74] D.J. Elliot, F. Pennella, J. Catal. 119 (1989) 359–367.
[75] J. Nakamura, J.A. Rodriguez, C.T. Campbell, Does J. Phys.: Condens. Matter 1 (1989) SB149–SB160.
[76] M.A. Henderson, Surf. Sci. Rep. 46 (2002) 1–308.
[77] A. Trunschke, D.L. Hoang, H. Lieske, J. Chem. Soc., Faraday Trans. 91 (1995) 4441–4444.